

Ultrafast Laser Processing On Transparent Materials

Antonios Papadopoulos



University of Crete

Master Thesis

Supervisor: Dr. Stratakis Emmanuel, Prof. Kioseoglou George

Department of Materials Science and Technology

October 2016

Abstract

Periodic structures in nano and micro scale were observed on transparent material surface after irradiating with femtosecond laser pulses. The periodicity of those structures can be manipulated by the fluence, the number of pulses and the wavelength of the incident beam. Also the orientation and morphological shape can be manipulated using a variety of polarizations such as linear, elliptical, circular, radial and azimuthal polarization. Taking advantage of that, complex structures can be produced aiming to create biomimetic surfaces which have similar properties with the subject.

ACKNOWLEDGEMENTS

I would like to express my special thanks to my supervisors Dr. Stratakis Emmanuel and Associate Professor George Kioseoglou, for giving me the opportunity to work on this project and guide my experimental work.

Also special thanks to MSc Evangelos Skoulas for the training and for the great collaboration we had to achieve our common goals, Dr. George Tsibidis who develop the theoretical framework to explain our experimental results, Alexandra Manousaki for the endless hours in Scanning Electron Microscopy, MSc Alexandros Mimidis for the collaboration we had despite our different projects and Andreas Lemonis for the technical support.

Finally I would like to thank all my colleagues Paraskevi, Kanelina, Chara, Ioannis, Epameinondas, Efthymis, Eleftheria, Ioanna, Despoina, Kyriaki, Maria, George M., George K., George S., Spyros, Andreas, Iakovos, Dimitrios, Kleitos, Sirago, Leonidas, Antonia, Christina, Konstantina, Anna-Maria, Athanasia for their support during my master.

Table of Contents

| | |
|---|----|
| List of Figures | 6 |
| List of Tables | 10 |
| List of abbreviations | 11 |
| CHAPTER 1: Introduction | 12 |
| 1.1 Theoretical background..... | 12 |
| 1.1.1 Ultrafast lasers | 12 |
| 1.1.2 Electromagnetic Radiation | 17 |
| 1.1.3 Transparent Materials | 18 |
| 1.1.4 Periodic structures (LIPPS) | 21 |
| 1.1.5 Biomimetics..... | 24 |
| 1.1.6 Aim of the Project..... | 26 |
| CHAPTER 2: Materials and Methods | 27 |
| 2.1 Materials..... | 27 |
| 2.2 Methods..... | 27 |
| 2.2.1 Ultraviolet-Visible Spectroscopy (UV-Vis) | 28 |
| 2.2.2 Scanning Electron Microscopy (SEM)..... | 29 |
| 2.2.3 Two Dimensional Fast Fourier Transform (2D-FFT) | 30 |
| 2.2.4 Fluence..... | 31 |
| 2.2.5 Pulse Duration | 32 |
| CHAPTER 3: Results and Discussion | 35 |
| 3.1 LIPSS in various types of transparent materials | 35 |
| 3.2 Manipulation of LIPPS Periodicity | 37 |
| 3.3 LIPSS as a Function of Pulse Duration (PD) | 43 |
| 3.4 Polarization Dependent LIPSS..... | 46 |

| | |
|-------------------------------|----|
| 3.5 Biomimetic surfaces | 49 |
| CHAPTER 4: Conclusions | 57 |
| List of references..... | 58 |

List of Figures

| | |
|--|----|
| Figure 1: Ultrafast laser parameters | 13 |
| Figure 2: a) Energy states of a semiconductor where the fermi energy is indicated. b) Electron stimulation where an electron absorbs a photon with energy larger than the band gab. c) Spontaneous emission. d) Stimulated emission. | 14 |
| Figure 3: Typical solid state laser set up..... | 14 |
| Figure 4: A variety of modes inside the cavity around the central wavelength of 1030 nm a) Random phases b) Lock phases. | 16 |
| Figure 5: Ultrafast laser set up. | 17 |
| Figure 6: An electromagnetic wave where blue is the magnetic field, red is the electric field and propagates along the black axis. | 17 |
| Figure 7: a) Linear polarization, b) Azimuthal polarization c) Radial polarization d) Elliptical polarization e) Circular polarization. | 18 |
| Figure 8: a) Multiphoton ionization b) Tunneling ionization [31] c) Avalanche ionization | 20 |
| Figure 9: Photoionization rate and Keldysh parameter as a function of laser intensity for 800 nm light in fused silica[31] | 21 |
| Figure 10: a) Relaxation mechanisms of the material and timelines after irradiation [33]. b) surface damage after the irradiation with long pulse laser beam and ultrafast laser pulses [34]. | 22 |
| Figure 11: SEM images (Top view) of a) HSFL after irradiation at 1026nm, RR=60 kHz, NP=30, Fl=0.7 Jcm² and PD=170 fs. b) LSFL after irradiation at 1026nm, RR=60 kHz, NP=20, Fl=2.7 Jcm² and PD=170fs. c) Grooves after irradiation at 513nm, RR=60 kHz, NP=20, Fl=2.4 Jcm² and PD=170fs. (The white double-ended arrow indicates the laser beam polarization) | 23 |
| Figure 12:(a) Photo of a glasswing butterfly (Greta oto) (b) The SEM image of the transparent region (c) SEM image of the area between microhairs (d) Reflection values are about 2% (two surfaces) for wavelengths between 390 and 700nm and increase up to 3% for 800 nm. (e) Angle dependent reflection measurment with an unpolarized focused laser light with 632.8nm wavelength [50]. | 25 |
| Figure 13: Processing set up | 27 |
| Figure 14: UV-Vis experemental set up. | 28 |

| | |
|--|----|
| Figure 15: Scanning Electron Microscopy set up. | 30 |
| Figure 16: a) SEM images (Top view) on fused silica surface after irradiation with $Fl=1.85 Jcm^2$ at 513nm for $NP=20$ and $PD=170$ fs. b) 2D-FFT image of the selected area. c) Profile of the white dashed line from image (b) (The double-ended arrow indicates the laser beam polarization). | 31 |
| Figure 17: Spot profile of the electromagnetic beam from CCD camera, focus by a spherical lens $f=60mm$ a) Top view b) Prospective view, c) Spot size of the imprint to Fused silica, focus by a spherical lens $f=150mm$ | 32 |
| Figure 18: Autocorrelator set up | 33 |
| Figure 19: Autocorrelator spectrum at compressor's position a) 135000 b) 180000 c) 220000 d) Pulse duration as a function of compressor's position. | 34 |
| Figure 20: SEM images (Top view) of LIPSS formation after irradiating with 5, 15 and 30 NP in a) Borosilicate glass b) Quarts c) Soda-lime glass d) Fused silica. (The white double-ended arrow indicates the laser beam polarization in all cases) | 36 |
| Figure 21: Fused Silica a) Periodic structure dependence on NP b) Fluence dependence of periodic structures for $NP=20$ (The red dash line indicates the wavelength of incident beam which is 1026nm). | 37 |
| Figure 22: SEM images (Top view) of fused silica after irradiation. Red arrows indicate the evolution of LIPPS under 1026nm irradiation and Green arrows under 513nm irradiation. Images are indicated by colors for HSFL (Blue), LSFL (Pink) and Grooves (Black). | 38 |
| Figure 23: A comparison of 1026nm and 513nm wavelength at $RR=60$ kHz and $PD=170$ fs for a) Fluence dependence of periodicity on fused silica b) NP dependence of periodicity on fused silica. | 39 |
| Figure 24: SEM images (Top view) of quarts after irradiation. Red arrows indicate the evolution of LIPPS under 1026nm irradiation and Green arrows under 513nm irradiation. Images are indicated by colors for HSFL (Blue), LSFL (Pink) and Grooves (Black). | 40 |
| Figure 25: a) Comparison of fluence dependence of periodicity at 1026nm, $RR=60kHz$ and $PD=170fs$ on fused silica ($a-SiO_2$) and quarts ($c-SiO_2$). b) Comparison of fluence dependence of periodicity at 513nm, $RR=60kHz$ and $PD=170fs$ on fused silica ($a-SiO_2$) and quarts ($c-SiO_2$) ... | 41 |
| Figure 26: SEM images (Top view) of Borosilicate glass after irradiation. Red arrows indicate the evolution of LIPPS under 1026nm irradiation and Green arrows under 513nm irradiation. Images are indicated by colors for HSFL (Blue), LSFL (Pink) and Grooves (Black). | 43 |

| | |
|--|----|
| Figure 27: Borosilicate glass a) Periodic structure dependence on NP b) Fluence dependence of periodic structures for NP=20 (The red dash line indicates the wavelength of incident beam which is 1026nm). | 43 |
| Figure 28: SEM images (Top view) of Fused silica after irradiation at 1026nm, NP=10 and RR=1kHz. Red arrows indicate the evolution of LIPPS as a function of Fluence and Pulse duration. Images are indicated by colors for HSFL (Blue), LSFL (Pink), Grooves (Black) and No structure formation (White) | 44 |
| Figure 29: SEM images (Top view) of Fused silica after irradiation at 1026nm, Fl=1.5 J/cm ² and RR=1kHz. Red arrows indicate the evolution of LIPPS as a function of Number of pulses and Pulse duration. Images are indicated by colors for HSFL (Blue), LSFL (Pink), Grooves (Black) and No structure formation (White)..... | 45 |
| Figure 30: SEM images (Top view) of Fused silica after irradiation at 1026nm, Fl=3.7 J/cm ² and RR=1kHz. Red arrows indicate the evolution of LIPPS as a function of Number of pulses and Pulse duration. Images are indicated by colors for HSFL (Blue), LSFL (Pink), Grooves (Black) and No structure formation (White)..... | 46 |
| Figure 31: SEM images (Top view) on fused silica surface after irradiation at 1026nm, 170fs and 1kHz repetition rate with a) linear polarization, Fl = 1.01 Jcm² , NP = 4 b) Elliptical polarization, Fl = 0.76 Jcm² , NP = 4. c) Azimuthal polarization, Fl = 3.97 Jcm² , NP = 4. d) Radial polarization, Fl=4.7 Jcm² , NP = 6..... | 47 |
| Figure 32: Periodicity dependence on NP and Fluence dependence of periodicity for azimuthal, radial and elliptical polarization..... | 48 |
| Figure 33: SEM images (Top view) on fused silica surface after irradiation at 1026nm and 60kHz repetition rate with linear polarization, Fl=0.7 Jcm² , NP=15 and PD = 170 fs. | 49 |
| Figure 34: a) SEM images (Top view) on fused silica surface after irradiation at 1026nm and 1kHz repetition rate with circular polarization, PD = 170 fs, Fl=12.57 Jcm² , NP=6 and b) 2D-FFT of image (a) | 50 |
| Figure 35: a) Nanopillars periodicity as a function of NP in vertical and horizontal direction. b) Nanopillar radius as a function of NP | 51 |
| Figure 36: SEM images (45° tilted) on fused silica surface after irradiation at 1026nm and 1kHz repetition rate with circular polarization, 170 fs pulse duration Fl=3.35 Jcm² , NP=10. | 52 |
| Figure 37: a) Damage spot during scanning b) Damage surface due to defects..... | 52 |

| | |
|--|----|
| Figure 38: a) Transmittance spectrum b) Reflectance spectrum c) SEM images (top view and 40° tilted) of the surfaces indicated by the respectively colors of the spectrums..... | 53 |
| Figure 39: a) Transmittance spectrum for single and double side processing b) Reflectance spectrum for single and double side processing c) SEM images (top view and 40° tilted) of the surfaces indicated by the respectively colors of the spectrums. | 54 |
| Figure 40: a) Transmittance spectrum for different number of scans b) Reflectance spectrum for different number of scans c) SEM images (top view and 40° tilted) of the surfaces indicated by the respectively colors of the spectrums. | 55 |
| Figure 41: SEM images (45° tilted) on fused silica surface after irradiation a) at $\lambda=513\text{nm}$ where $\Lambda=376\pm35$ the periodicity, 52 ± 10 the radius and 156 ± 27 the height of nanopillars. b) at $\lambda=1026\text{nm}$ where $\Lambda=393\pm20$ the periodicity, 85 ± 17 the radius and 282 ± 42 the height of nanopillars. | 56 |

List of Tables

| | |
|--|----|
| Table 1: Transparent materials and applications | 19 |
| Table 2: Types of LIPSS observed in various types of transparent materials | 36 |

List of abbreviations

| | |
|------------------|--|
| LIPSS | Laser-induced periodic surface structure |
| HSFL | High-spatial-frequency-LIPSS |
| LSFL | Low-spatial-frequency-LIPSS |
| CW | Continuous Wave |
| ev | Electronvolt |
| SEM | Scanning Electron Microscopy |
| UV | Ultraviolet |
| Vis | Visible |
| IR | Infrared |
| Fs | Femtosecond (10^{-15} s) |
| Ps | Picosecond (10^{-12} s) |
| Ns | Nanosecond (10^{-9} s) |
| PD | Pulse Duration |
| RR | Repetition Rate |
| NP | Number of pulses |
| Fl | Fluence |
| 2D-FFT | Two Dimensional Fast Fourier Transform |
| STE | Self-trapped exciton |
| FWHM | Full Width Half Maximum |
| BPO ₄ | Boron phosphate |

CHAPTER 1: Introduction

During last decades the technology of Ultrafast laser has grown rapidly in a way that from the original nanosecond laser [1] to reach an attosecond laser [2]. Due to the short pulse duration, high peak power and broad spectral bandwidth properties of an ultrafast laser, it has a wide range of applications such as micromachining, Rapid Scanning Time Delays for Ultrafast Measurement, Electro-Optic Sampling and Field Mapping, Terahertz Wave Imaging, Communication Systems, Nonlinear Microscopy and Ophthalmology among others [3]. Focusing on the micromachining applications, laser-induced periodic surface structure (LIPSS) was first introduced by Birnbaum in 1965 [4]. Since then many studies have been conducted to explain the phenomenon in metals [5-8], semiconductors [9-12] and dielectrics [13-15]. Transparent materials with their known optical properties such as transparency and reflectance are particularly interesting systems to be process by lasers in order to explore the effects on their properties for a variety of possible applications. Those materials can therefore transformed into Superhydrophobic or Superhydrophilic surfaces, Colorized surfaces and Bioinspired surfaces (Biomimetics) among others. More over the optical properties of transparent materials can be adjusted by lasers in order to achieve the specifications set by industries and laboratory research.

1.1 Theoretical background

1.1.1 Ultrafast lasers

By the term ultrafast laser we refer to pulsed lasers where the electromagnetic pulse duration is in the order of a picosecond (10^{-12} second) or less. Since the first generation of ultrashort optical pulses by Mocker and Collins [1], ultrafast lasers have attracted the interest of the scientific community due to its small pulse duration and high peak power which often leads to nonlinear interactions with materials. The two important parameters used to describe ultrafast lasers are pulse duration (PD) and repetition rate (RR). As shown in Fig. 1 pulse duration is the duration of the electromagnetic pulse in time and the repetition rate is the frequency of pulse occurrence.

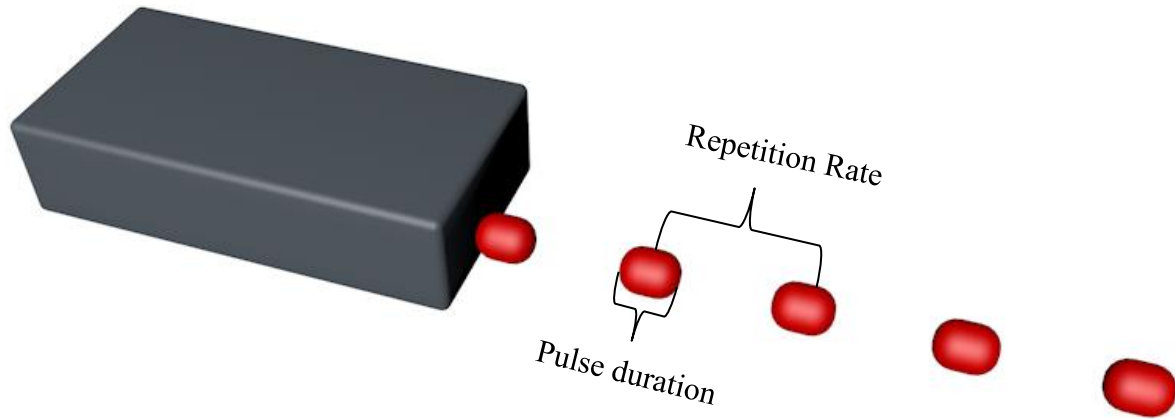


Figure 1: Ultrafast laser parameters

1.1.1.1 Basic Theory

The basic component of solid state lasers is a semiconductor. Semiconductors can behave as insulators or conductors depending on the operation conditions due to the energy band gap that separates the conduction band from the valence band as shown in Fig 2. The electron distribution in a semiconductor follows the Fermi–Dirac distribution which depends on the temperature:

$$F(E) = \frac{1}{1 + e^{\frac{E-E_f}{k_B T}}}$$

where $F(E)$ is the probability of an electron to be in the energy state E , E_f is the fermi energy which is the highest occupied energy state and it depends on the electron density, $k_B = 1.38 \cdot 10^{-23} \frac{J}{K}$ is the Boltzmann constant and T is the temperature. When the fermi energy is between the conduction and valence band then only the valence band is occupied and the probability of an electron to be in the conduction band is small. So when an incident electromagnetic wave with energy $h\nu > \text{band gap}$ interacts with a semiconductor, an electron from the valence band can absorb the energy and be stimulated in the conduction band as shown in Fig. 2B. Then spontaneous emission occurs where the electron from the conduction band decays to the valence band emitting a photon with the same energy as the electron transition as shown in Fig 2C. The interaction of an electromagnetic wave with a semiconductor can also produce the stimulated emission where the incident photon forces an electron to decay from the conduction band and emit a photon with the same energy as the incident photon as shown in Fig 2D. The stimulated emission is the operating principle of laser and requires population inversion by an external source of energy, where the number of electrons in

the conduction band exceeds the number of electrons in the valence band so that the probability of a stimulated emission to be higher than the electron stimulation.

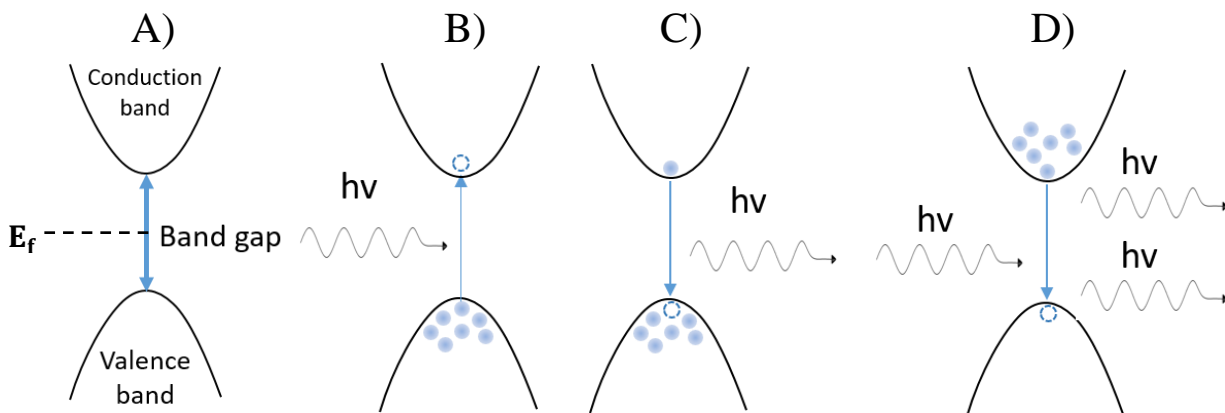


Figure 2: a) Energy states of a semiconductor where the fermi energy is indicated. b) Electron stimulation where an electron absorbs a photon with energy larger than the band gab. c) Spontaneous emission. d) Stimulated emission.

A simple laser set up is shown in Fig. 3 where the medium in solid state lasers is a semiconductor. When the population inversion begins, first by spontaneous emission, a photon is emitted. Then amplification takes place through the stimulated emission while the light oscillates inside the cavity due to mirror placement. Absorbing material is used in order to absorb the light that does not have the direction of the cavity. That allows the production of a spatial coherence beam. Finally the light escapes from the mirror with the lower reflectivity in order to produce the output beam.

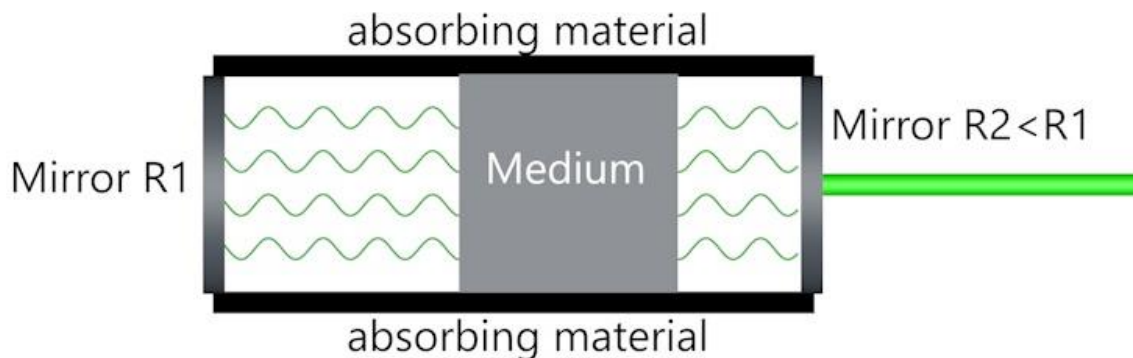


Figure 3: Typical solid state laser set up.

1.1.1.2 Pulsed lasers

The light that is emitted by a simple laser is a continuous wave (CW) irradiation. In order to produce an optical pulse in the ultrafast time scale, a technique called Mode-locking was proposed by Lamp and Willis [16]. In this case the medium is able to give photons with slightly different wavelength (modes) around the central wavelength where the individual phase of the light waves in each mode is random. The difference in the setup between a simple CW laser and an ultrafast laser is the use of a saturable absorber [17] or an optical modulator [18]. A saturable absorber selectively absorbs low-intensity light and transmit light with sufficiently high intensity. Ultrafast lasers are able to lock the phases of the different electromagnetic waves so that the modes of the laser will periodically all constructively interfere with one another to give pulsed irradiation output as shown in Fig. 4b. The distance between the pulses (repetition rate) is $\Delta\nu = \frac{2L}{c}$ where L is the distance between the mirrors of the cavity and c is the speed of light.

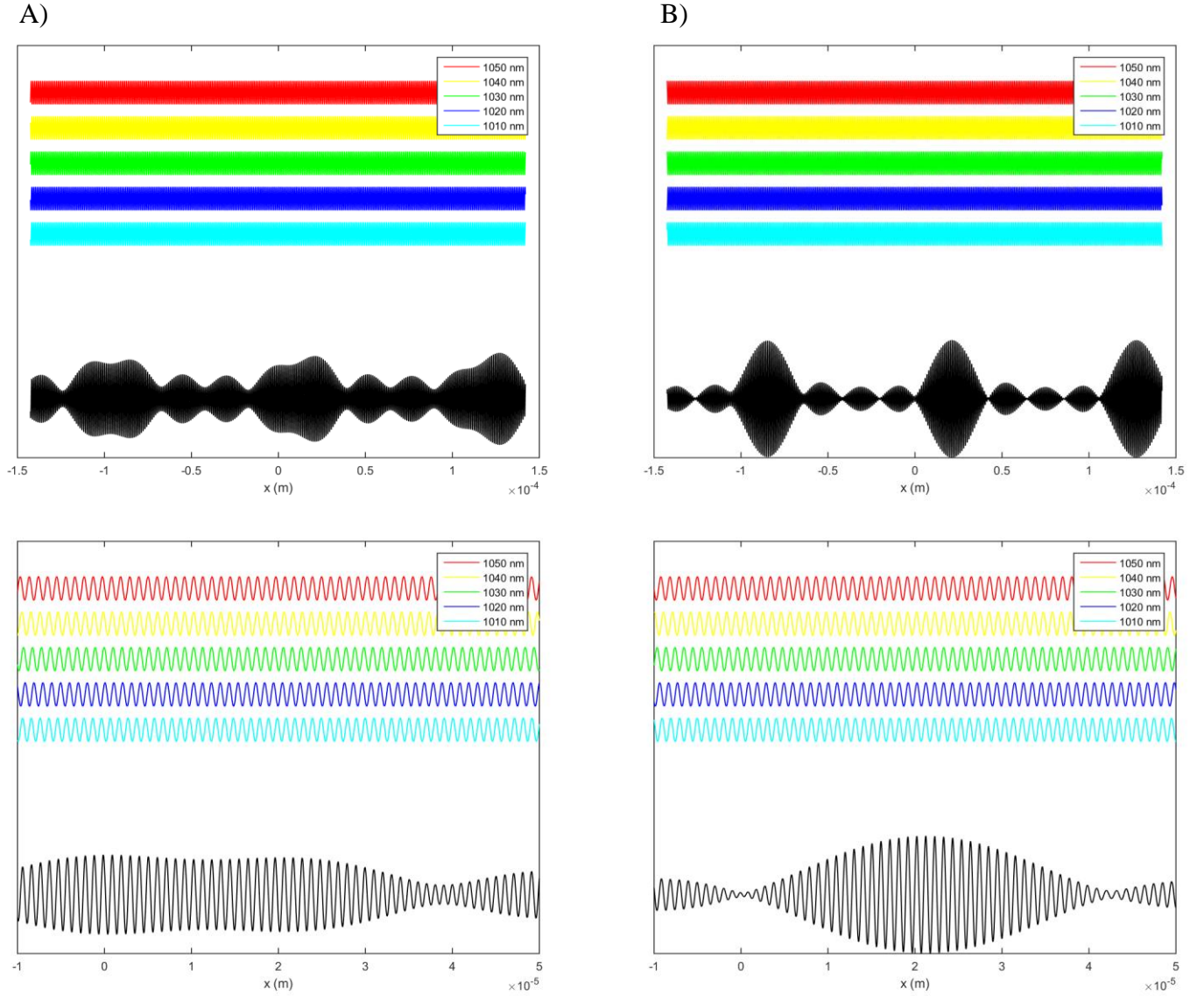


Figure 4: A variety of modes inside the cavity around the central wavelength of 1030 nm a) Random phases b) Lock phases.

1.1.1.3 Amplification

In order to increase the output power of the laser, an amplification is needed through stimulated emission using a gain medium. However, due to the concentration of energy at such a short time, the high peak power of amplified pulses may damage the medium [3]. To prevent the damage a technique called chirped pulse amplification was introduced in 1985 by Strickland et al. in the field of ultrafast optical pulses [19]. This technique requires to stretch the pulses out in time taking advantage of the group velocity dispersion and self-phase modulation where the propagation of

light in a medium differs depending on the wavelength. Then the stretched pulse can be safely amplified and finally compressed using a pair of gratings as shown in Fig 5.



Figure 5: Ultrafast laser set up.

1.1.2 Electromagnetic Radiation

Electromagnetic radiation is essentially elementary particles called photons. It is a wave that comprised of electric and magnetic fields in synchronized oscillations that propagate at the speed of light in vacuum as shown in Fig. 6. The energy of a photon is

$$E = h \cdot \nu$$

$$\nu = \frac{c}{\lambda}$$

where h is the Planck's constant, ν is the frequency of the wave, c is the speed of light and λ is the wavelength.

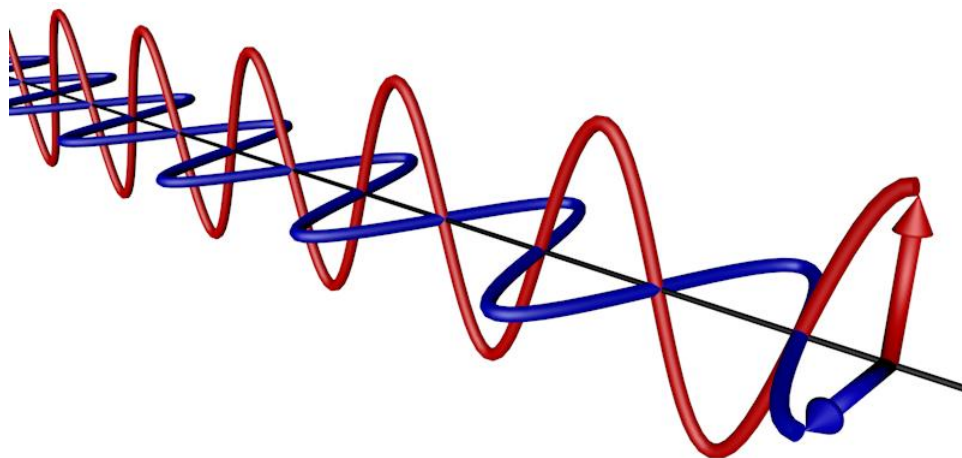


Figure 6: An electromagnetic wave where blue is the magnetic field, red is the electric field and propagates along the black axis.

The polarization of the laser radiations refers to the vector of the electric field. There are different kinds of polarization. For this project linear, elliptical, circular, radial and azimuthal polarization were used.

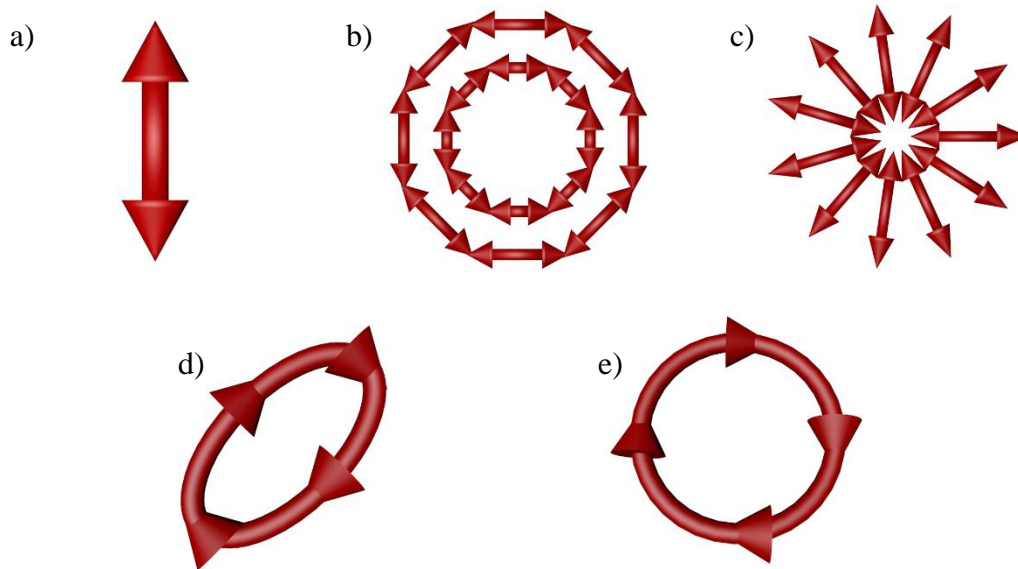


Figure 7: a) Linear polarization, b) Azimuthal polarization c) Radial polarization d) Elliptical polarization e) Circular polarization.

1.1.3 Transparent Materials

A transparent material is basically any material that has high transmittance in the UV-Vis-IR spectrum. Taking advantage of this property, transparent materials are widely used in our daily life for windows in buildings and vehicles, screen protectors, houseware, laboratory equipment etc. The process of those materials using ultrafast lasers and the introduction of LIPPS on the surface can improve or change the properties of the material to suit a specific application.

Table 1: Transparent materials and applications

| Material | Properties | Applications |
|--------------------|--|---|
| Fused Silica | Amorphous structure SiO_2 , bandgap = 7.46 - 9.56 eV [20], Density = 2.2 g/cm ³ [21], refractive index \approx 1.4 [22] | Fiber optics [23] lenses, incandescent tungsten halogen lamps, solar cell covers, windows for space vehicles, mirror blanks, thin-film dielectric coating in integrated circuits [21] |
| Soda lime glass | Amorphous structure of $\sim 72\%$ SiO_2 , $\sim 13\%$ Na_2O and $\sim 8\%$ CaO [24]. Density = 2.47 g/cm ³ [21], refractive index \approx 1.5 [25] Band gap = 5.6 eV [26] | Solar collectors, in passive solar-heating systems [21] |
| Borosilicate glass | Amorphous structure of B_2O_3 and SiO_2 , Density = 2.13-2.48 g/cm ³ [21] Band gap = 4.28 eV [27] | Ovenware, laboratory equipment, piping, sealed-beam headlights, in glass fibers for reinforcement, textile, insulation fiber. [21] |
| Quartz | Crystal structure SiO_4 , bandgap = 8.05 - 9.55 eV [20], refractive index \approx 1.5 [28] | Piezoelectric applications [29] |

1.1.3.1 Laser – Matter Interaction

The energy band gap of transparent materials is usually larger than 3 eV, as shown in table 1, which means that they do not absorb energy through photoionization when irradiating in Vis-IR spectrum because the photon energy is smaller than the energy bandgap. Nevertheless under intense irradiation other mechanisms can describe the interaction of light with transparent materials such as multiphoton ionization, tunneling ionization and avalanche ionization.

Multiphoton ionization is a process where electrons from the valance band can absorb simultaneously more than one photon under strong electromagnetic irradiation. The electrons excite to a number of virtual states and finally to the conduction band as shown in Fig 8a.

Tunneling ionization occurs when the intensity of the incident electromagnetic irradiation is high enough to distort the potential energy of atoms. So electrons from the valance band can easily stimulate to the conduction band through tunnel ionization as shown in Fig 8b [30].

In the case of *avalanche ionization*, excited free electrons, from multiphoton or tunneling ionization, in the presence of electric field can accelerate and collide with atoms in the lattice as

shown in Fig. 8c. When the kinetic energy of the accelerated electron is higher than the energy bandgap of the material then ionization occurs. The stimulated electrons from the collision can accelerate and ionize more atoms.

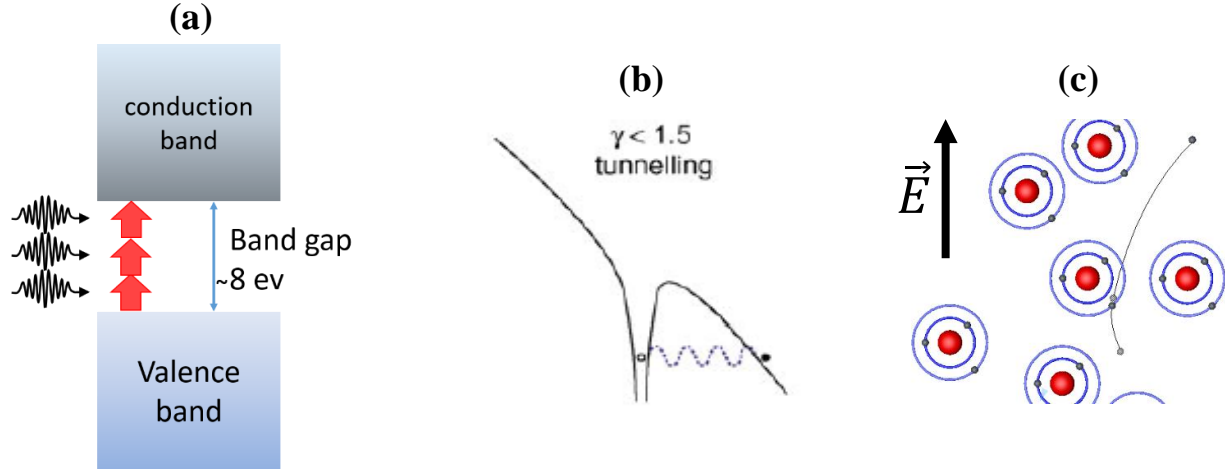


Figure 8: a) Multiphoton ionization b) Tunneling ionization [31] c) Avalanche ionization

Depending on the laser frequency and intensity, there are three different regimes on how a material can absorb energy through multiphoton ionization or tunneling ionization. The first regime refers to multiphoton ionization only, the second regime refers to tunneling ionization only and the third regime refers to simultaneously multiphoton and tunneling ionization as shown in Fig. 9. To predict the regime of absorption, Keldysh equation could describe the phenomenon.

$$\gamma = \frac{\omega}{e} \left(\frac{m \cdot c \cdot n \cdot \epsilon_0 \cdot E_g}{I} \right)^{1/2}$$

where γ is the Keldysh's parameter, ω is the laser frequency, I is the laser intensity at the focus, m is the reduced mass, e is the charge of the electron, c is the speed of light, n is the refractive index of the material, E_g is the band-gap of the material and ϵ_0 is the permittivity of free space. The Keldysh's parameter can indicate the regime which is tunneling ionization for $\gamma < 1.5$, multiphoton ionization for $\gamma > 1.5$ and a combination of the two for $\gamma = 1.5$ [31].

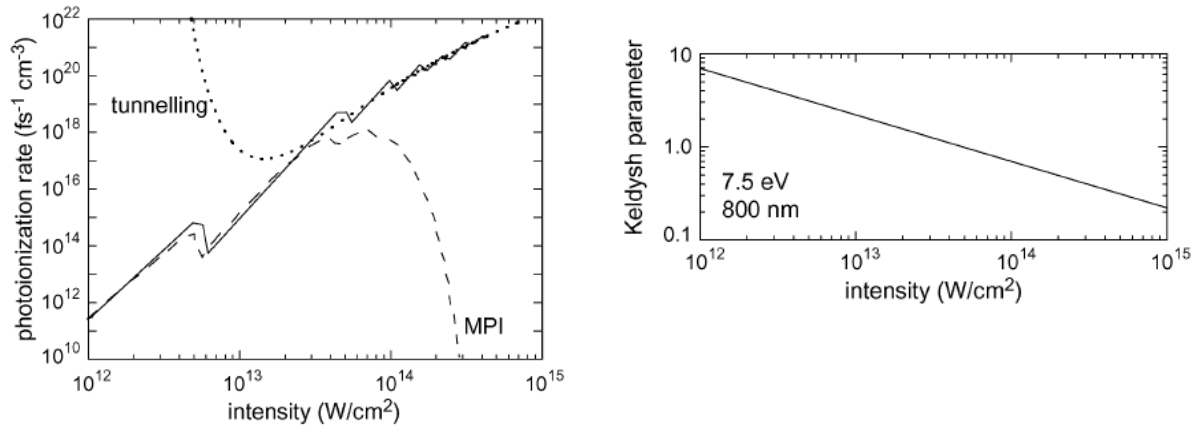


Figure 9: Photoionization rate and Keldysh parameter as a function of laser intensity for 800 nm light in fused silica[31]

1.1.4 Periodic structures (LIPPS)

Immediately after the irradiation and excitation of electrons, the relaxation process takes place with a variety of mechanisms and timescales as shown in Fig. 10a. The energy is being transferred from the excited carrier (excited electrons) to lattice at a time scale of sub-picosecond after the irradiation through carrier-carrier scattering and carrier-phonon scattering mechanisms. Continuing, the excited carriers start to decay 10^{-11} seconds after irradiation through the carrier removal process. At the same time heat is diffused from the material's surface to the bulk causing ablation and evaporation and hence the material evaporate or melt depending on the energy deposition from the irradiation. Ablation occurs when atoms acquire enough kinetic energy for individual atoms, ions, molecules or clusters to detach from the material. Finally the material resolidified 10^{-9} seconds after the irradiation.

So by using ultrafast lasers with pulse duration less than sub-picosecond, we can limit the thermalization and thermal diffusion, caused by the relaxation process, in order to avoid the ablation of clusters and evaporation of material and to encourage the formation of periodic structures in micro and nano scale [32].

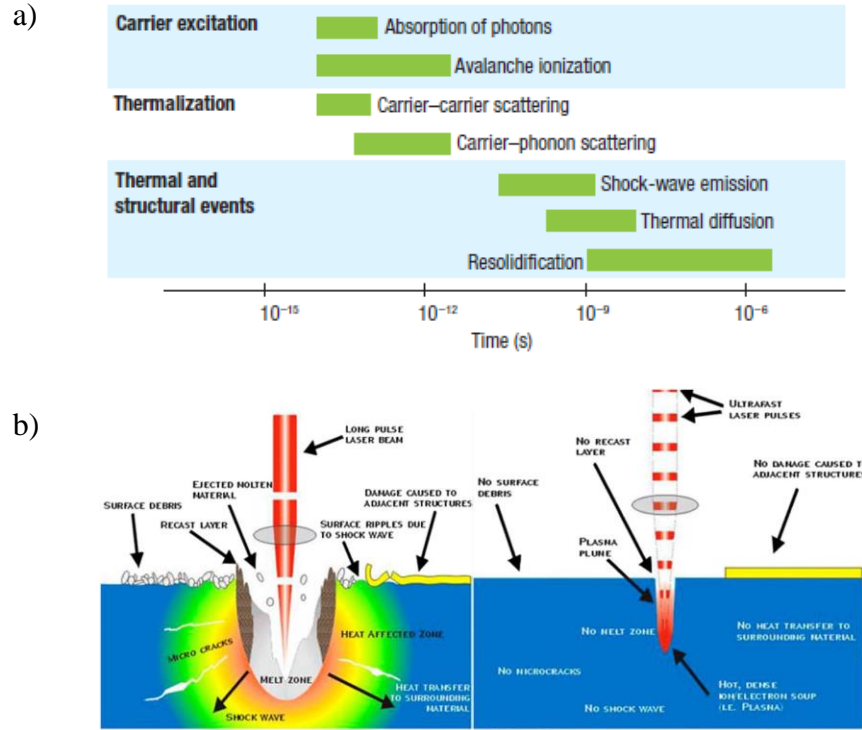


Figure 10: a) Relaxation mechanisms of the material and timelines after irradiation [33]. b) surface damage after the irradiation with long pulse laser beam and ultrafast laser pulses [34].

There are three types of LIPSS that have been observed so far in the surface of transparent materials after irradiation named **HSFL**[35-37], **LSFL** [35-37] and **Grooves** [38, 39] as shown in Fig. 11. HSFL are high spatial frequency periodic structures where the periodicity is half or less than the wavelength of the incident beam and the direction is perpendicular to the incident polarization. LSFL are low spatial frequency periodic structures where the periodicity is near the wavelength and are parallel to the polarization of the incident beam. Finally Grooves are periodic structures where the periodicity is higher even multiple times the incident wavelength and the direction is parallel to the polarization.

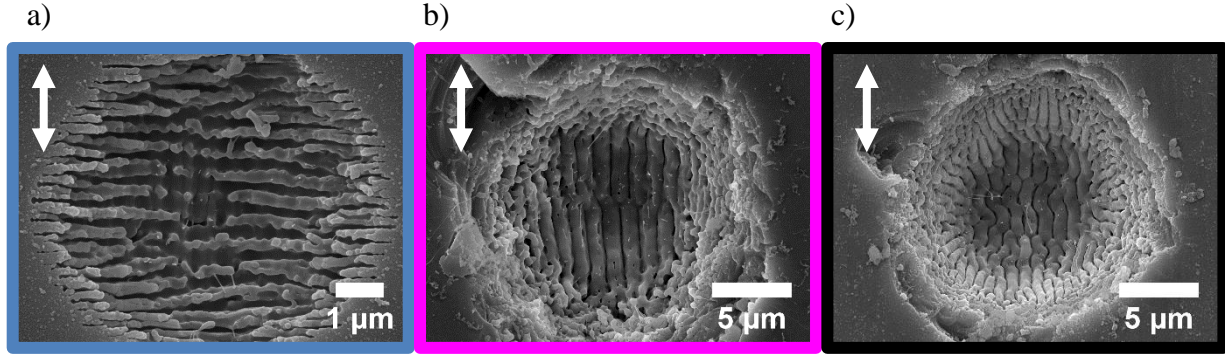


Figure 11: SEM images (Top view) of a) HSFL after irradiation at 1026nm, RR=60 kHz, NP=30, FI= $0.7 \frac{J}{cm^2}$ and PD=170 fs. b) LSFL after irradiation at 1026nm, RR=60 kHz, NP=20, FI= $2.7 \frac{J}{cm^2}$ and PD=170fs. c) Grooves after irradiation at 513nm, RR=60 kHz, NP=20, FI= $2.4 \frac{J}{cm^2}$ and PD=170fs. (The white double-ended arrow indicates the laser beam polarization)

The mechanism that leads to the formation of LIPSS in transparent materials is controversial. A few attempts have been made to explain the phenomenon on transparent materials such as Maragoni convection[38, 40], surface plasmon polariton [41] and grating-assisted enhanced energy deposition and the subsequent thermal effects [41] but none of them can explain the formation of grooves.

Our proposed mechanism by D.Tsibidis et al. [39] focuses on the excited electron density and electron-lattice heat diffusion model coupled with Navier-Stokes equations [42]. Due to the high number of excited electrons after irradiation, the material acquires metallic characteristics and thus a Two Temperature Model can describe the spatio-temporal dependence of the temperatures:

$$C_e \frac{\partial T_e}{\partial t} = \vec{\nabla} \cdot (K_e \cdot \vec{\nabla} T_e) - \frac{C_e}{\tau_E} \cdot (T_e - T_L) + S(\vec{x}, t)$$

$$C_L \frac{\partial T_L}{\partial t} = \frac{C_e}{\tau_E} \cdot (T_e - T_L)$$

where T_e is the carrier temperature, T_l is the lattice temperature, C_e is the heat capacity of electrons, C_l is the heat capacity of lattice, k_e is the thermal conductivity of the electrons, τ_E is the energy relaxation time for the liquid phase, t is time and $S(\vec{x}, t)$ is the source. To represent the excitation of electrons after irradiation, the multiple rate equation [43] was revised to take into

account self-trapped exciton (STE) states and free electron relaxation. Self-trapped exciton is an incubation effect where a small fraction of excited electrons do not recombine but they are stabilized into additional energy levels caused by defects inside the material. Also the initial multiple rate equation assumes that all excited electrons participate in avalanche ionization and ignores the free electron relaxation which reduces the free electron density. The deposition of optical energy in the material is proportional to

$$n(k) \times |b(k)|$$

where η is the efficacy factor at k and b is the surface roughness at k . Efficacy factor refers to the ability of the material to absorb optical energy where the surface roughness leads to inhomogeneous absorption of radiation the result of which is the formation of LIPSS. Summarizing, LIPSS with periodicity smaller or equal to wavelength appears for small free electron densities due to inhomogeneous absorption of laser light below material's rough surfaces. Grooves appear for large number of excited electron densities. The increased temperature due to relaxation process leads to thermal gradient and the formation of convection rolls in the molten material because of the Marangoni effect which eventually leads to grooves. The direction of convection rolls is parallel to the original LSFL as described by the large Prandtl number in molten dielectrics [44-46].

1.1.5 Biomimetics

Biomimetics or biomimicry is the imitation of biological systems in the laboratories. The aim of biomimetics is to reproduce similar structures in the lab with the target biological system in order to adapt their useful properties. Examples of successful biomimicry are the super-hydrophobic surfaces of lotus leaf [47], biomimetic materials for tissue engineering [48] and polymers for Biomimetic Sensors [49].

An example of a possible biomimetic surface on transparent materials is the glasswing butterfly Greta Oto whose transparent region of the wing has anti-reflection properties. Its wings feature three regions such as transparent, dark brown and white. The transparent region is covered with $\sim 2\mu\text{m}$ thick and $\sim 40\mu\text{m}$ long bristles or microhairs and the areas between these microhairs are covered with nanopillars as shown in Fig. 3c. The nanopillars, that give an anti-reflection behavior to the material, are irregularly arranged and have a random height and width distribution [50].

Antireflective surfaces can be used to improve the light collection in solar cells or to enhance the performance of the optical, optoelectronic and electro-optical devices [51-53].

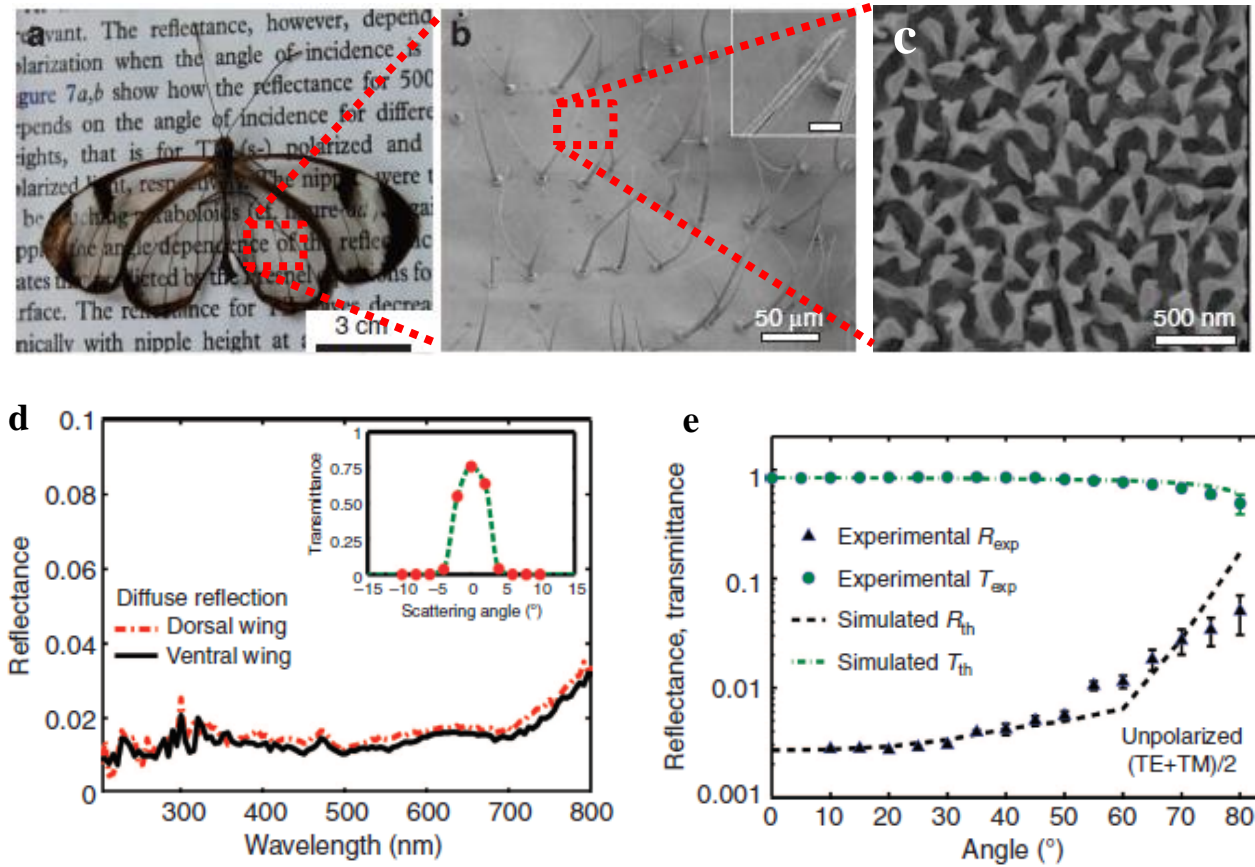


Figure 12:(a) Photo of a glasswing butterfly (Greta oto) (b) The SEM image of the transparent region (c) SEM image of the area between microhairs (d) Reflection values are about 2% (two surfaces) for wavelengths between 390 and 700nm and increase up to 3% for 800 nm. (e) Angle dependent reflection measurement with an unpolarized focused laser light with 632.8nm wavelength [50].

According to the analysis of the transparent region that has been done by Siddique et al., the periodicity of nanopillars is 100-140 nm, the radius is 40-60 nm and their height is 160-200 nm. The optical analysis showed that the reflectance is about 2% in the visible regime, 3% at near IR regime and at the same time the material is more than 80% transparent at 633nm wavelength [50].

1.1.6 Aim of the Project

The aim of this project is to develop controlled periodic structures in nano and micro scale using ultrafast pulsed laser processing on the surface of transparent materials for a variety of potential applications such as Superhydrophobic or Superhydrophilic surfaces, Lithography, Coloring surfaces, Bioinspired surfaces (Biomimetics) and materials with adjustable optical properties.

CHAPTER 2: Materials and Methods

2.1 Materials

Commercial UV-Grade Fused Silica ($n_d = 1.45846$, $d = 2.2 \frac{g}{cm^3}$) with 1 mm thickness and double side polished was purchased from GPO, Germany.

Commercial Soda-lime glass with 1 mm thickness and Borosilicate glass with 0.6mm thickness, double side polished was purchased from Waldemar Knittel Glasbearbeitungs- GmbH, Germany

Commercial Quartz glass with 1 mm thickness and double side polished was purchased from Apex Optical Services.

2.2 Methods

A Ytterbium-doped: potassium, gadolinium, tungstate (Yb:KGW) laser source was used to generate linearly polarized pulses with pulse duration from 170fs to 10ps, 1-200 kHz repetition rate and 1026nm or 513nm central wavelength. The laser beam was focused with a spherical lens ($f=60\text{mm}$ or $f=150\text{mm}$). All irradiations conducted in air environment under normal incidence where samples were positioned perpendicular to the incident beam and on a 3-axis motorized stage as shown in Fig. 13.

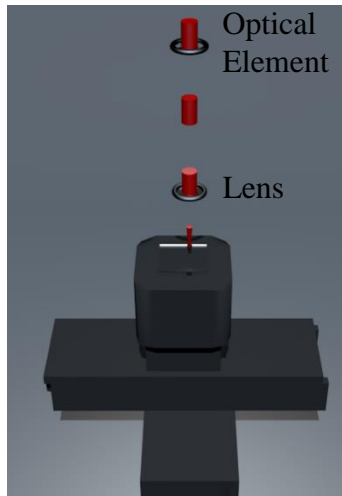


Figure 13: Processing set up

2.2.1 Ultraviolet-Visible Spectroscopy (UV-Vis)

UV-Vis spectroscopy is used to analyze the optical properties of processed transparent materials and compare them to the flat untreated material. From the optical analysis such as transmittance, absorbance and reflectance we can extract information about the changes in the optical properties of a material due to LIPSS structures. The sample is being scanned in different wavelengths within ultraviolet, visible and infrared radiation. A light source is used to generate a CW light in a wide range of wavelengths. Then the light pass through a monochromator where only one specific wavelength at the time can be transmitted. In the case of transmittance measurements, the sample is placed before the detector and in the case of reflectance measurements the sample is placed after the detector. The remaining irradiation that hasn't transmitted or reflected, is absorbed by the material.

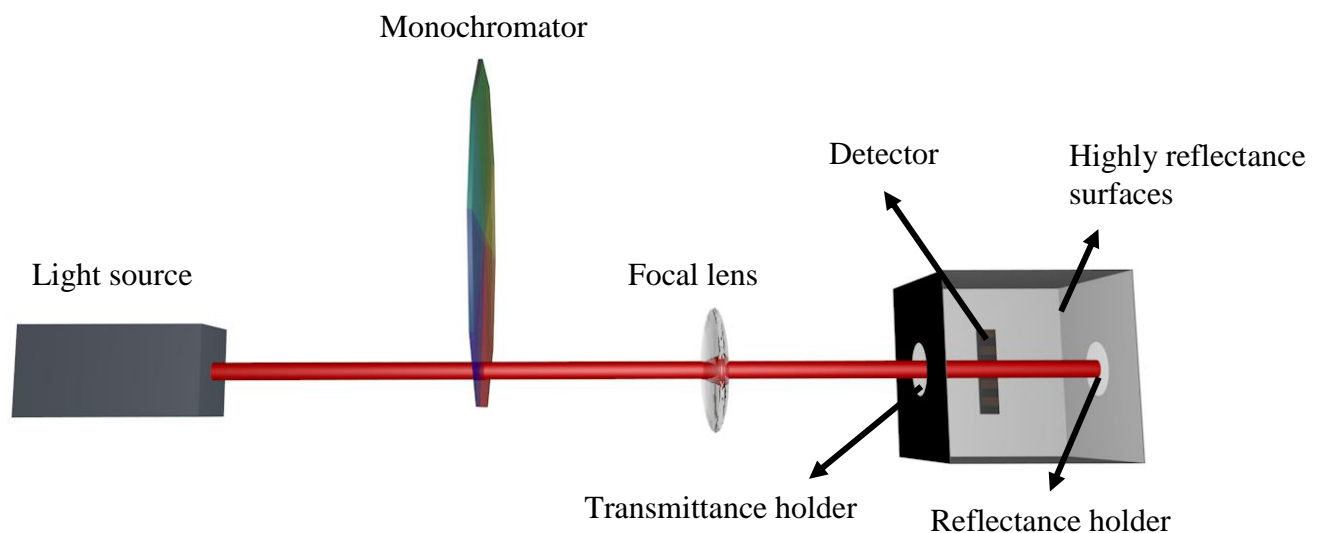


Figure 14: UV-Vis experimental set up.

2.2.2 Scanning Electron Microscopy (SEM)

SEM (JEOL JSM-7500F and JEOL JSM-6380) was used to visualize the processed surface after the irradiation. SEM is the most suitable method to visualize and analyze the LIPPS in micro and nano scale due to the fact that the resolution power of SEM can reach the nanometer scale.

$$\delta = \frac{0.61 \cdot \lambda}{\mu \cdot \sin(\beta)}$$

$$\lambda = \frac{h}{\sqrt{2 \cdot m_0 \cdot e \cdot V}} \text{ for electrons}$$

δ is the resolution power, λ is the wavelength, μ is reflective index of medium, β is semi-angle of collection of the magnifying lens, h is the Planck constant, m_0 is the electron mass, e is the electron charge and V is the voltage. In our case the operation voltage was set to 15kV and thus the theoretical resolution power is $\delta \approx 0.006 \text{ nm}$

The operation principle is the production of an electron beam from a filament. The beam is guided through an anode which cuts off the diffused electrons. Then electromagnetic lenses guide and focus the beam in the sample in order to interact and produce backscatter electrons and secondary electrons which are electrons extracted from the atoms of the sample. The two types of electrons are being detected from a scintillator material which absorbs the energy from the electrons and emits photons. So in order to form the final image the area is being scanned by the electron beam, guided by the electromagnetic lenses, to form the image pixel by pixel where the brightness of the pixel depends on the intensity of the electrons absorbed by the scintillator material.

For the visualization of transparent materials, a thin film of gold of approximately 30nm thickness was deposited in the surface using sputtering.

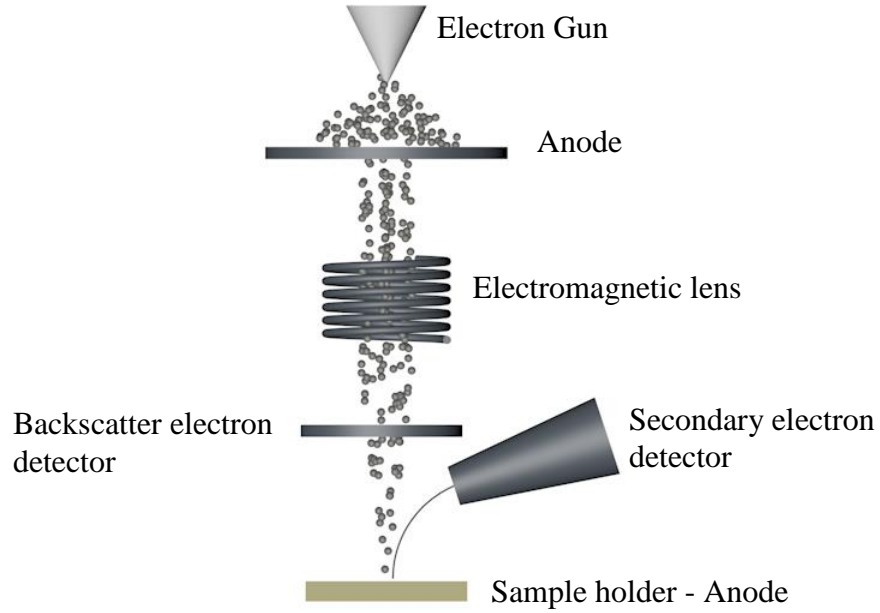


Figure 15: Scanning Electron Microscopy set up.

2.2.3 Two Dimensional Fast Fourier Transform (2D-FFT)

2D-FFT was used to calculate the periodicity of LIPSS. The periodicity is a very important parameter as it gives us information on the periodic structure's dimension. The dimension of LIPSS is one of the parameter that can affect the properties of the surface after the irradiation. SEM images were then analyzed using a 2D-FFT to calculate the periodicity as shown in Fig.16. The 2D-FFT image (Fig. 16b) of the original image reveals the direction of the periodicity which in this case is horizontal and thus the profile of the image was taken appropriately as shown in Fig. 16b with the white dash line. The distance between the central peak and peak 1 or 2 in Fig. 16c represents the frequency f of the periodic structure. In order to calculate the periodicity, Λ , of the structures first we calculate the average frequency from the distance of peaks *central-1* and *central-2*, and so the average period is $\langle \Lambda \rangle = \frac{1}{f}$. The error of every analysis is calculated as follows.

$$\Delta \Lambda = \left| -\frac{1}{f^2} \right| \cdot \Delta f$$

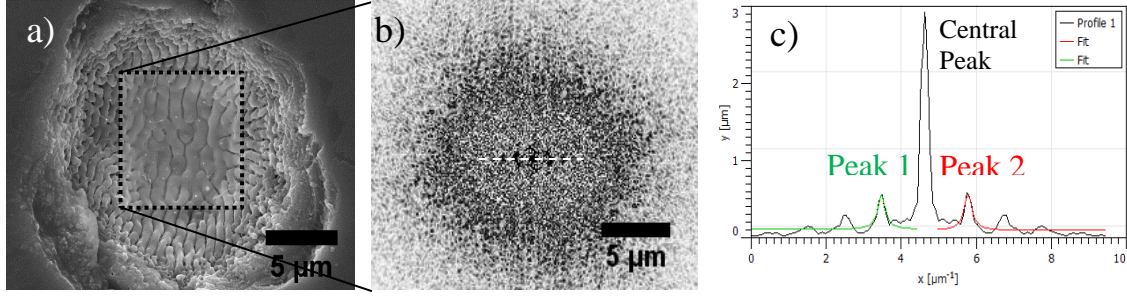


Figure 16: a) SEM images (Top view) on fused silica surface after irradiation with $Fl=1.85 \frac{J}{cm^2}$ at 513nm for NP=20 and PD=170 fs. b) 2D-FFT image of the selected area. c) Profile of the white dashed line from image (b) (The double-ended arrow indicates the laser beam polarization).

2.2.4 Fluence

Fluence is a universal parameter to express the energy deposition to the material from one electromagnetic pulse. Fluence is the energy per area and is calculated as follows

$$Pulse\ energy = \frac{Power\ (Watt)}{Repetition\ rate\ \left(\frac{1}{s}\right)}$$

$$Fl = \frac{Pulse\ energy\ (J)}{Spot\ Size\ or\ Area\ (cm^2)} = \left[\frac{J}{cm^2} \right]$$

The spot size is calculated either from a CCD camera or from the imprint to the material as shown in Fig. 17. The spot size is always calculated at $\frac{1}{e^2}$ as shown in Fig 17a. As we can see from the image in Fig.a,b the spatial profile of the beam is Gaussian.

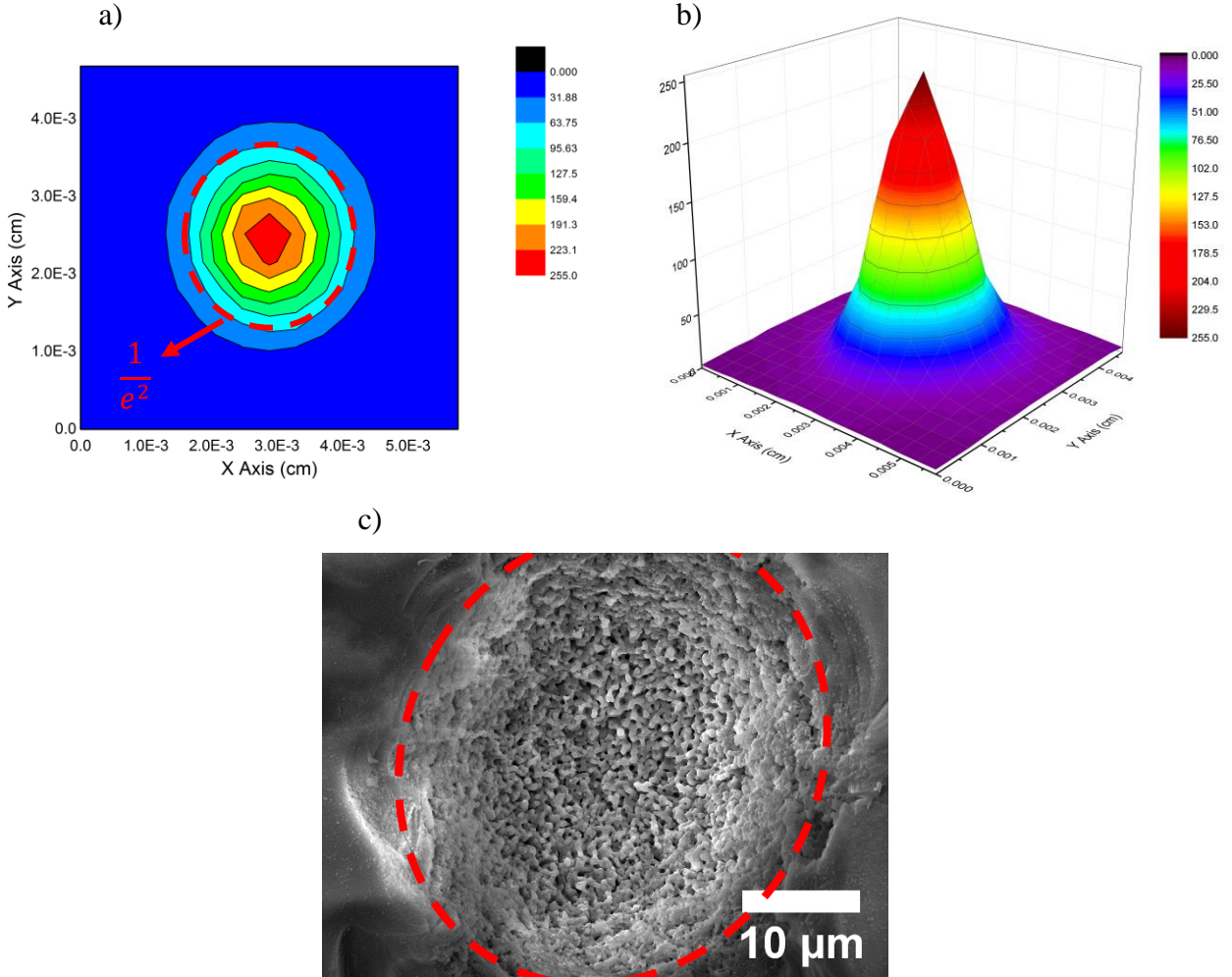


Figure 17: Spot profile of the electromagnetic beam from CCD camera, focus by a spherical lens $f=60\text{mm}$ a) Top view b) Prospective view, c) Spot size of the imprint to Fused silica, focus by a spherical lens $f=150\text{mm}$.

2.2.5 Pulse Duration

In order to measure the pulse duration, an interferometric autocorrelator set up was used as shown in Fig. 18. The incident beam is splitted 50:50 and each of the new beams is being reflected by a mirror. One of the two mirrors is placed on a motorized stage in order to create delay between the pulses from the two splitted beams by increasing or decreasing the optical path of one of the two beams. The two beams reunite and focus on a nonlinear crystal BPO_4 to generate second harmonics in order to enhance the signal. Finally a filter blocks the incident beam to let the photodiode detect only the second harmonics irradiation.

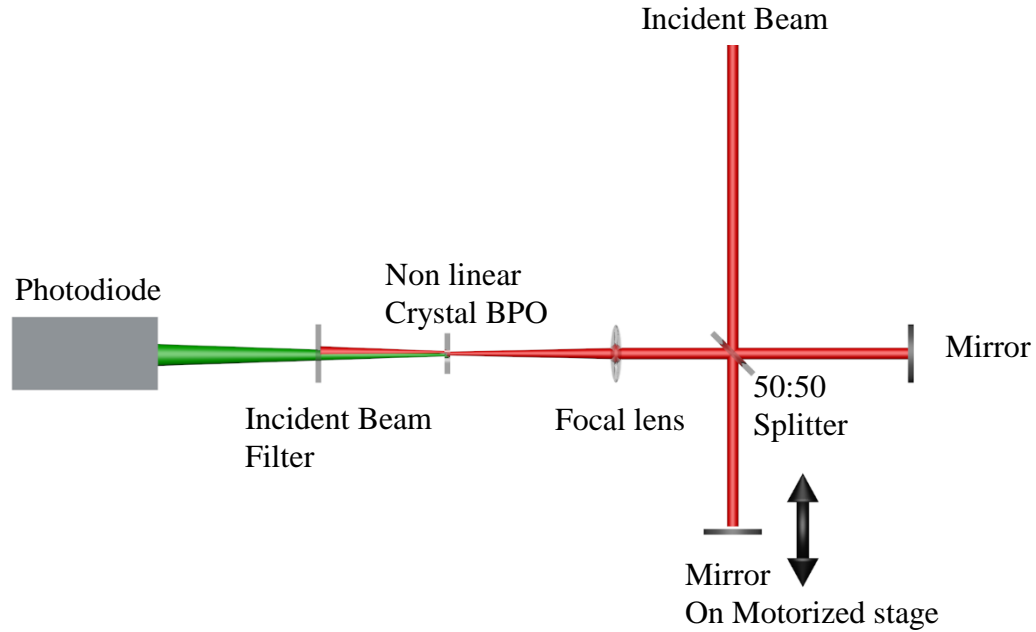


Figure 18: Autocorrelator set up

The positioning of the stage is determined in fs. In order to transform distance to time the speed of light was used

$$c = 3.00 \cdot 10^8 \frac{m}{s}$$

Therefore 1 fs corresponds to 0.3 μm . From the autocorrelator results the pulse duration is calculated at the 0.65*FWHM of the Gaussian fit. Three measurements were conducted where the compressor was set to different positions. As presented in Fig. 19d the pulse duration increases as the compressor's motor position increases. It was found that for the position 135000, 180000 and 220000 of the compressor the pulse duration is calculated to be (103 ± 11) fs, (5.3 ± 0.1) ps and (9.9 ± 0.3) ps respectively. The divergence of the autocorrelator data from the theoretical data, given by the laser manufacturing company, might be due to the set up imperfections, temperature variations, humidity variations and pulse stretching that occurs due to group velocity dispersion while propagating through optical elements.

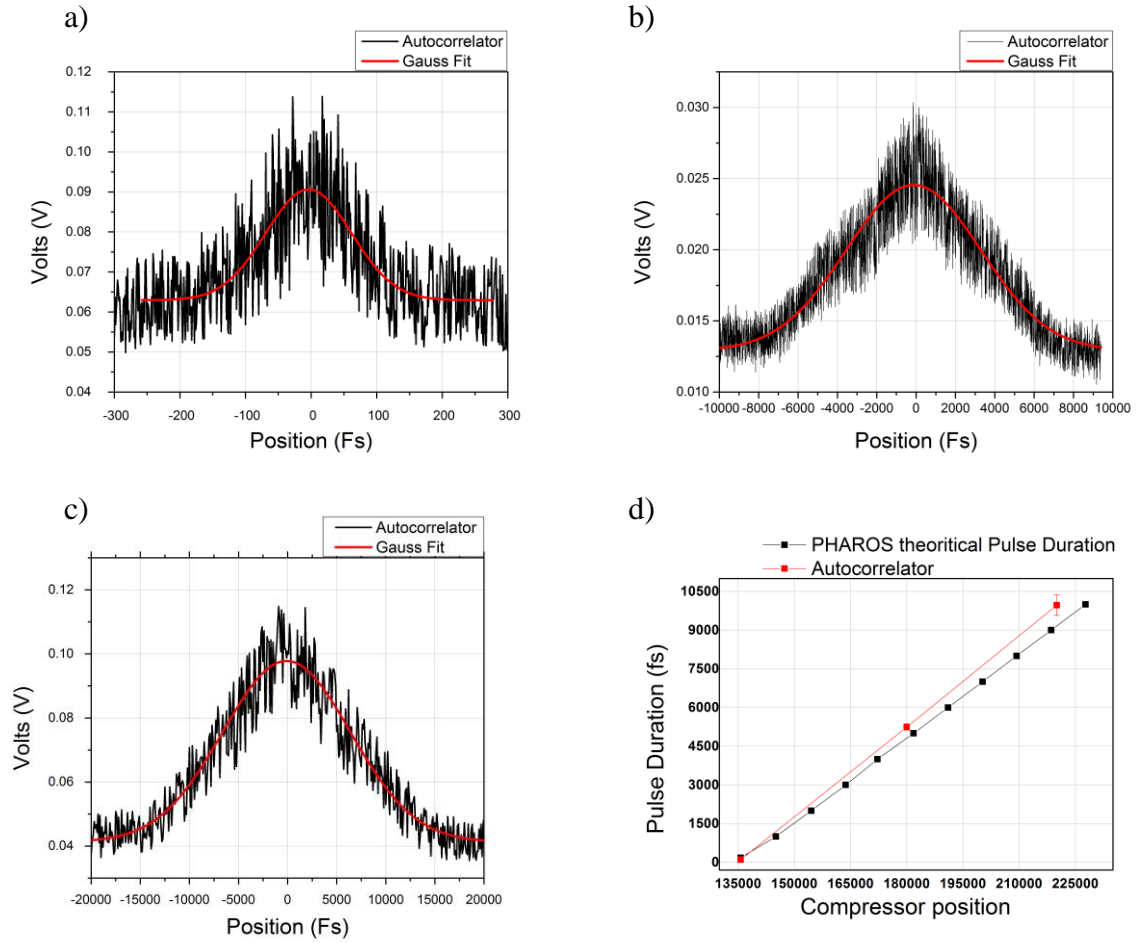


Figure 19: Autocorrelator spectrum at compressor's position a) 135000 b) 180000 c) 220000 d) Pulse duration as a function of compressor's position.

CHAPTER 3: Results and Discussion

3.1 LIPSS in various types of transparent materials

Periodic structures have been observed in different types of transparent materials. The fabrication of periodic structures in various transparent materials is important as it can give a variety of options to choose from when looking for the most suitable material for a specific application. Following on that, experiments have been conducted on Borosilicate glass, Soda-lime glass, Fused silica and Quarts and the results are presented below. Also experiments have been conducted on Polymethyl methacrylate (PMMA) and Polycarbonate but no periodic structures were formed.

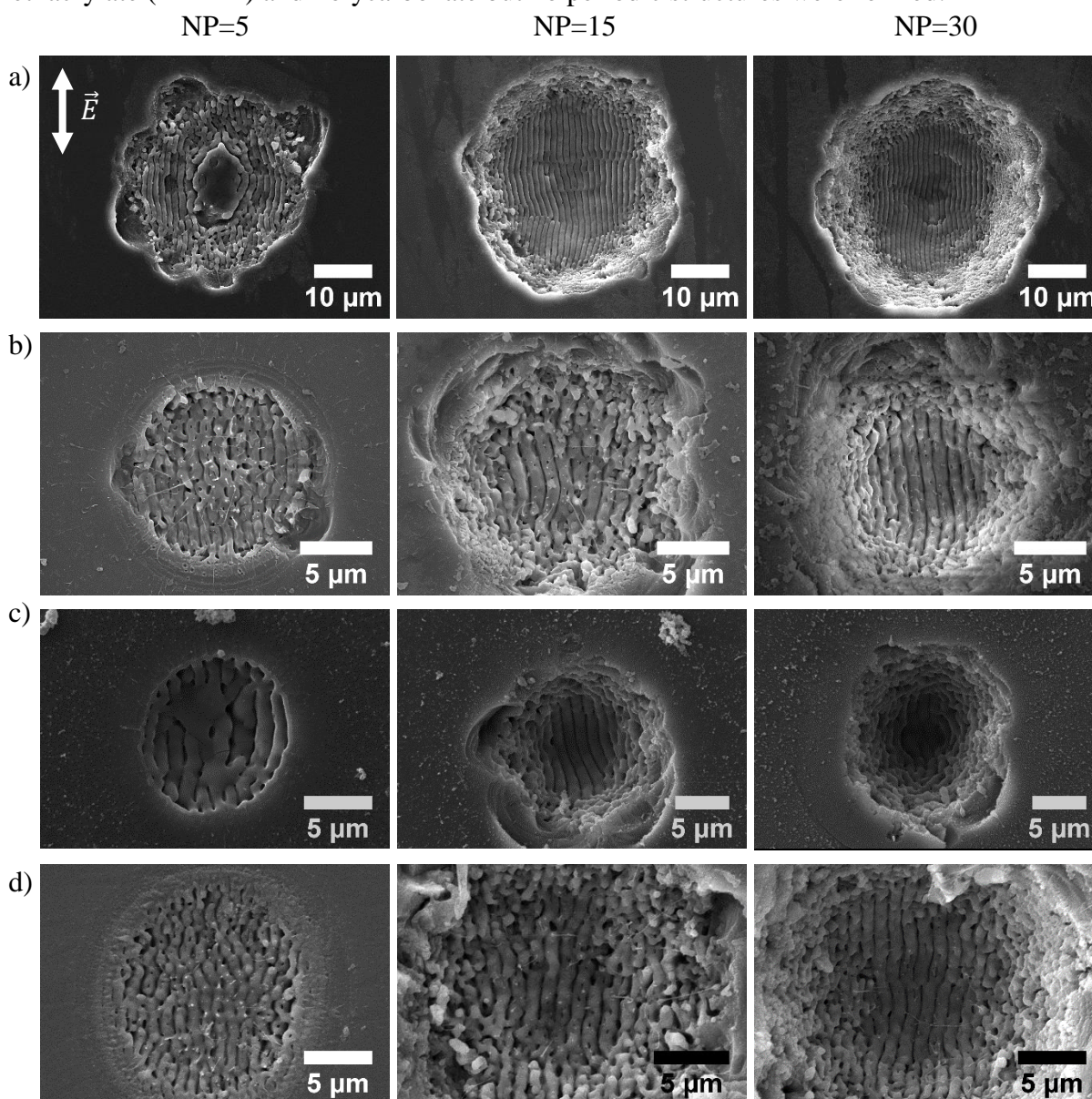
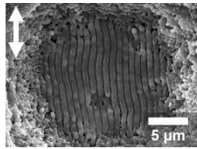
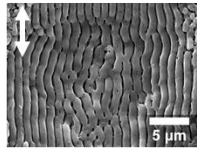
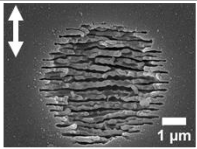
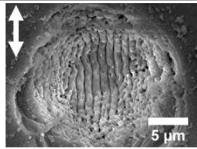
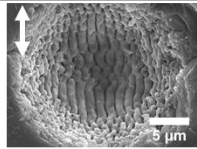
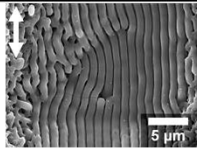
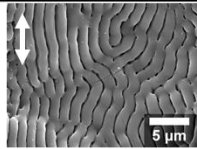
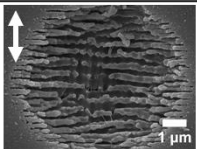
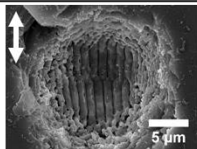
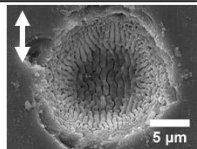


Figure 20: SEM images (Top view) of LIPSS formation after irradiating with 5, 15 and 30 NP in a) Borosilicate glass b) Quarts c) Soda-lime glass d) Fused silica. (The white double-ended arrow indicates the laser beam polarization in all cases)

All types of LIPSS except from HSFL have been observed on various types of transparent materials as shown in table 2. HSFL observed only in Fused Silica and Quartz due to the limited window of fluences that HSFL formed. Borosilicate glass and Soda-lime glass have smaller band gap compare to Fused Silica and Quartz and so the energies required to form HSFL are near the damage threshold.

Table 2: Types of LIPSS observed in various types of transparent materials

| | High Spatial Frequency LIPSS (HSFL) $\Lambda \leq \lambda/2$ | Low Spatial Frequency LIPSS (LSFL) $\Lambda \sim [\lambda/n, \lambda]$ | Grooves $\Lambda > \lambda$ |
|----------------------|---|--|---|
| Borosilicate Glass | ? |  |  |
| Quartz (c-SiO) |  |  |  |
| Soda-lime Glass | ? |  |  |
| Fused Silica (a-SiO) |  |  |  |

3.2 Manipulation of LIPPS Periodicity

As mentioned above in § 2.2.3 the periodicity is a very important parameter. In this project we were able to manipulate the periodicity by changing the number of pulses, the fluence and the wavelength of the incident beam. For Fused silica the periodicity usually increases as the number of pulses increases from 4 to 15 where the periodicity reaches a saturation point. Also as the fluence increases the periodicity increases. At small fluences there is only a HSFL formation and the direction of the periodicity is perpendicular to the polarization of the incident beam. As the fluence increases LSFL appears. However, usually at small NP there is also formation of HSFL along the perimeter of the spot, due to the Gaussian spatial shape of the pulse and the low energy deposition at the perimeter. Finally at high fluences we have the formation of Grooves due to the high number of excited electrons and during the relaxation process the material melts and form convection rolls which eventually lead to the formation of Grooves as discussed in § 1.1.4

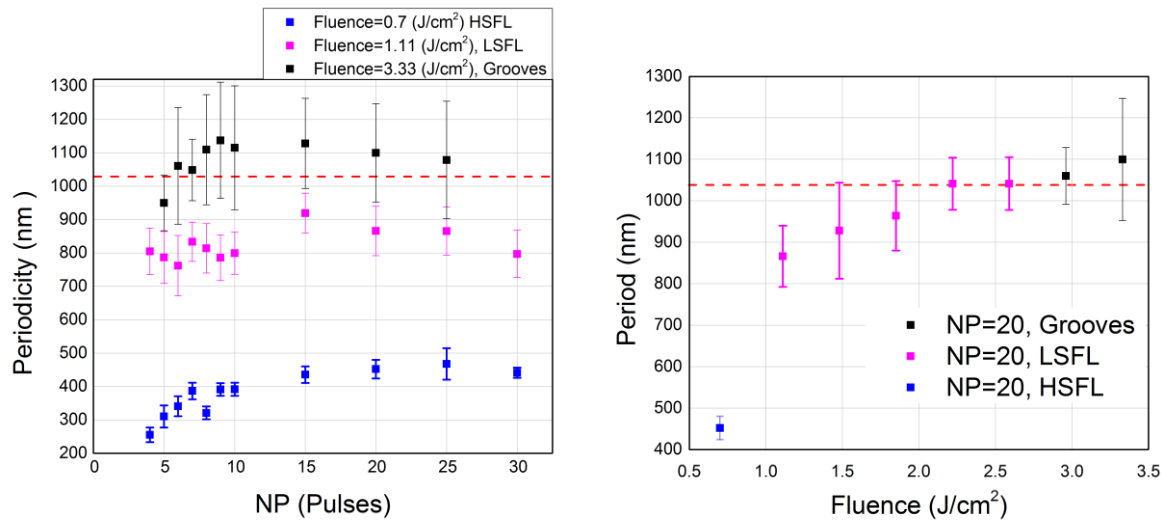


Figure 21: Fused Silica a) Periodic structure dependence on NP b) Fluence dependence of periodic structures for NP=20 (The red dash line indicates the wavelength of incident beam which is 1026nm).

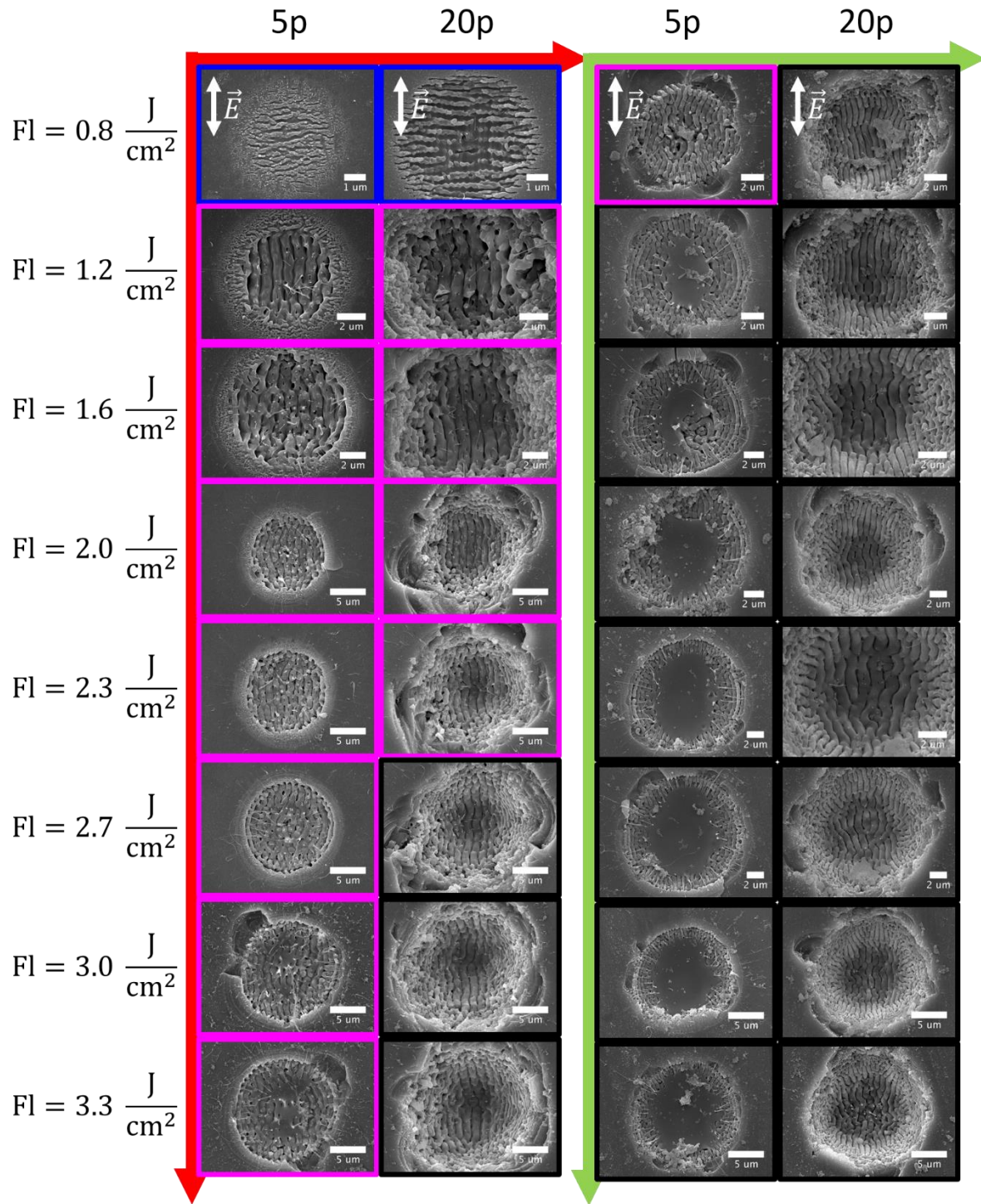


Figure 22: SEM images (Top view) of fused silica after irradiation. Red arrows indicate the evolution of LIPPS under 1026nm irradiation and Green arrows under 513nm irradiation. Images are indicated by colors for HSFL (Blue), LSFL (Pink) and Grooves (Black).

Continuing, the periodicity between two different wavelength at 1026nm and 513nm was compared. There's clearly a difference in the periodicity for different wavelengths. Specifically it is higher for the 1026nm compared to 513nm LIPSS. It is remarkable that in the case of 513nm irradiation we observe only the formation of grooves even for small fluences. After irradiating at 1026nm we observe the formation of near-wavelength structures or LSFL periodicities while at 513nm the periodicities exceed by far the wavelength. This phenomenon can be explained by the higher photon energy for 513nm which eventually leads to larger number of excited electrons.

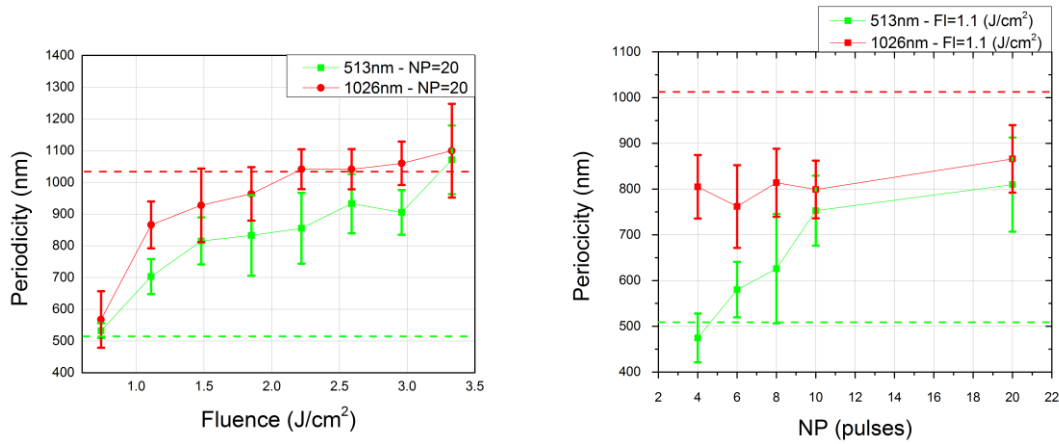


Figure 23: A comparison of 1026nm and 513nm wavelength at RR=60 kHz and PD=170 fs for a) Fluence dependence of periodicity on fused silica b) NP dependence of periodicity on fused silica.

A comparison of the behavior of a-SiO₂ and c- SiO₂ when irradiating with 1026nm and 513nm wavelength was conducted. No significant differences have been observed on the periodicity in the case of 1026nm as shown in Fig. 25 which means that the crystallinity of the silicon oxide does not affect the energy absorption. On the other hand regarding the irradiation at 513nm there is a slightly increment in the calculated periodicity of a-SiO₂ compared to c-SiO₂, as shown in Fig. 25 which means that the convection rolls, when the material melts, are affected by the chemical structure of the material.

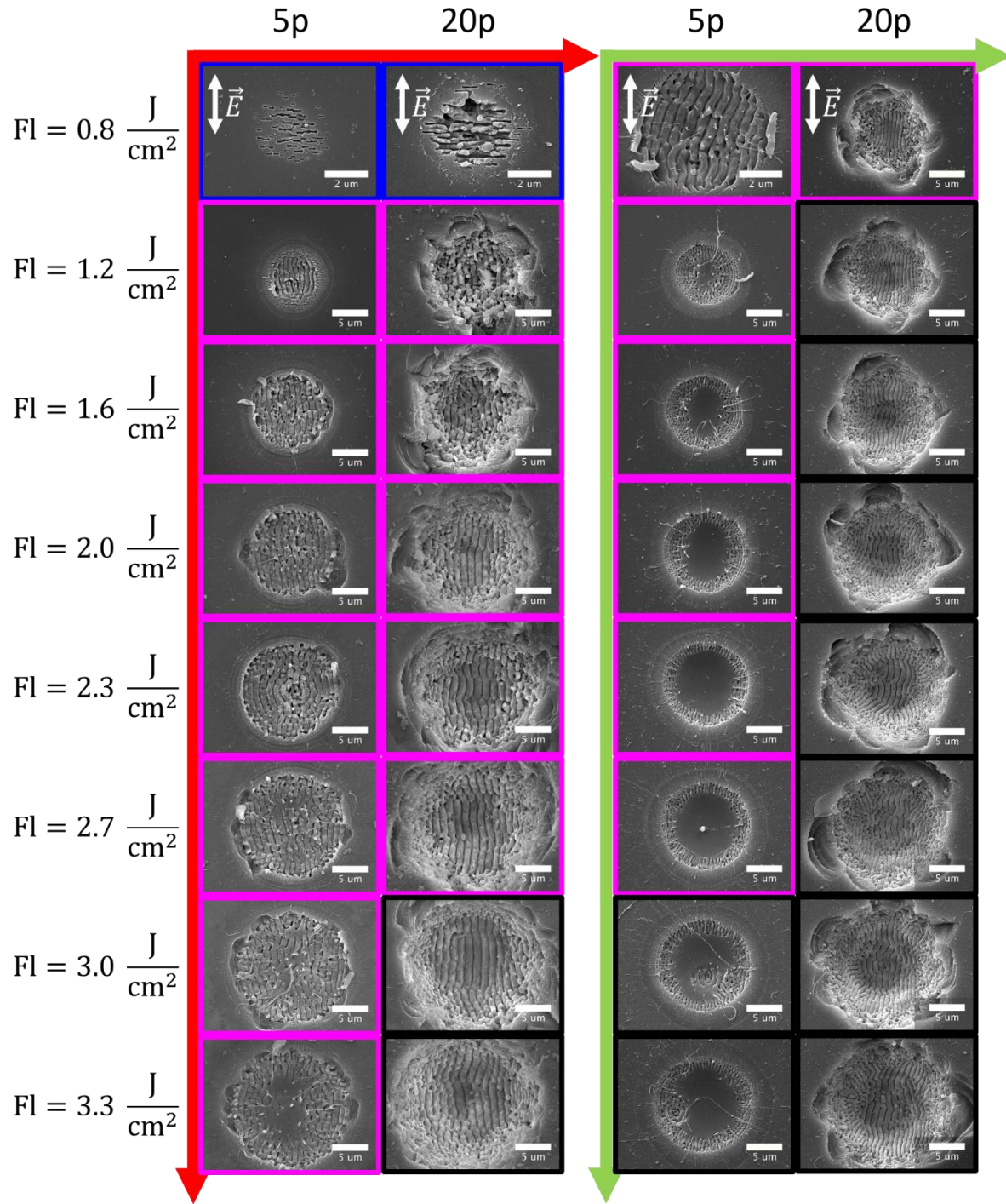


Figure 24: SEM images (Top view) of quarts after irradiation. Red arrows indicate the evolution of LIPPS under 1026nm irradiation and Green arrows under 513nm irradiation. Images are indicated by colors for HSFL (Blue), LSFL (Pink) and Grooves (Black).

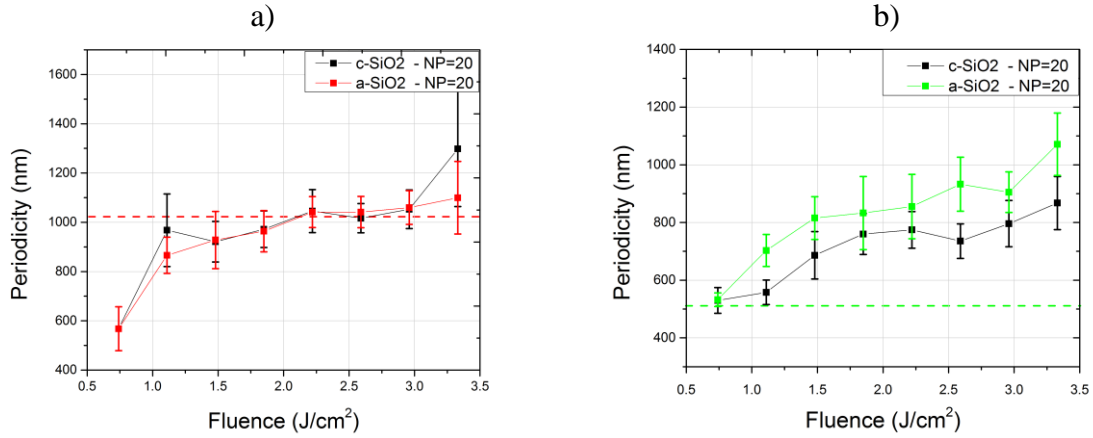


Figure 25: a) Comparison of fluence dependence of periodicity at 1026nm, RR=60kHz and PD=170fs on fused silica (a-SiO₂) and quartz (c-SiO₂). b) Comparison of fluence dependence of periodicity at 513nm, RR=60kHz and PD=170fs on fused silica (a-SiO₂) and quartz (c-SiO₂)

Finally the periodicity was examined for the case of borosilicate glass. The behavior in this case is different compared to fused silica and quartz as the periodicity increases to reach a peak and then decreases as the number of pulses increases. The same behavior is observed for the periodicity as a function of fluence.

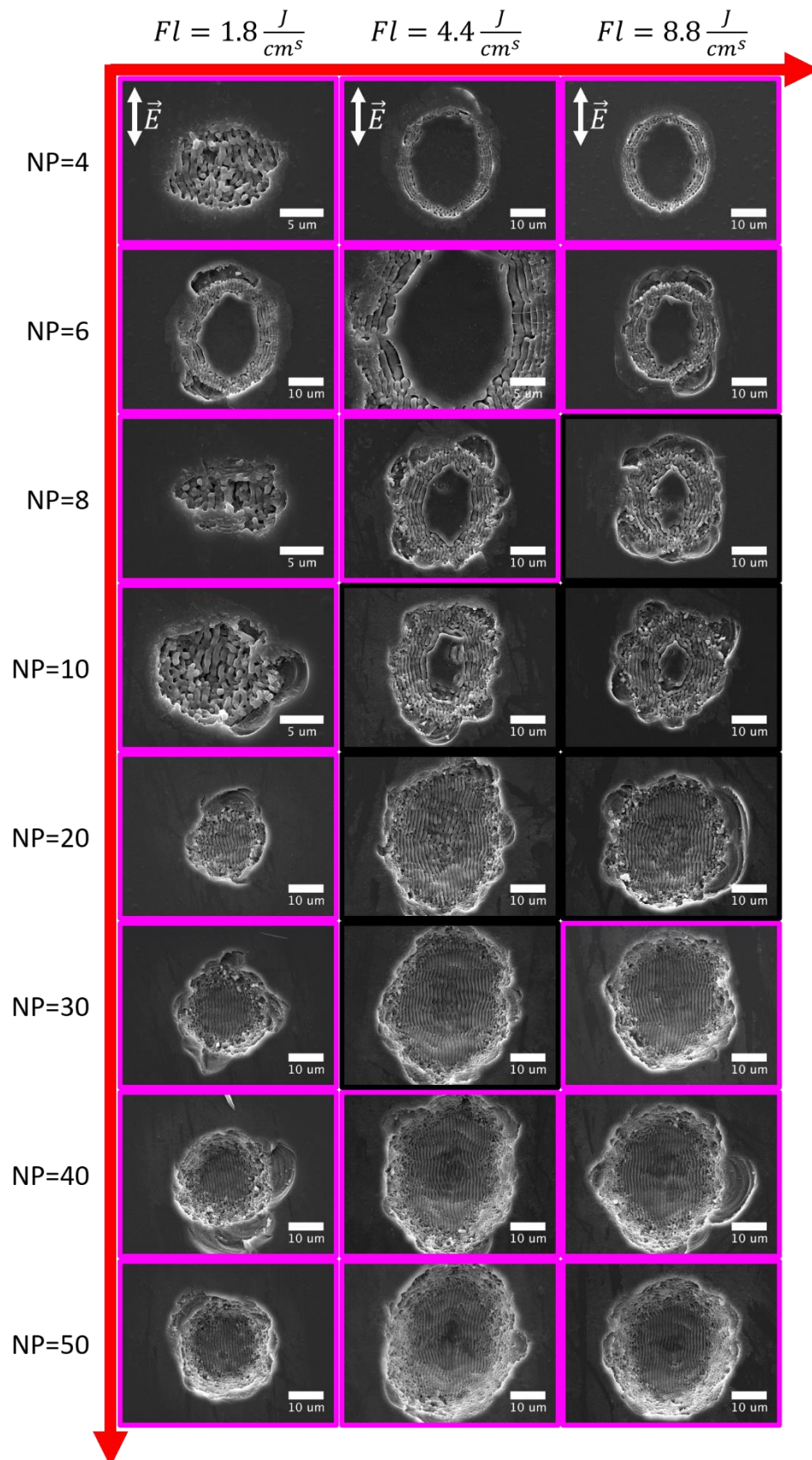


Figure 26: SEM images (Top view) of Borosilicate glass after irradiation. Red arrows indicate the evolution of LIPSS under 1026nm irradiation and Green arrows under 513nm irradiation. Images are indicated by colors for HSFL (Blue), LSFL (Pink) and Grooves (Black).

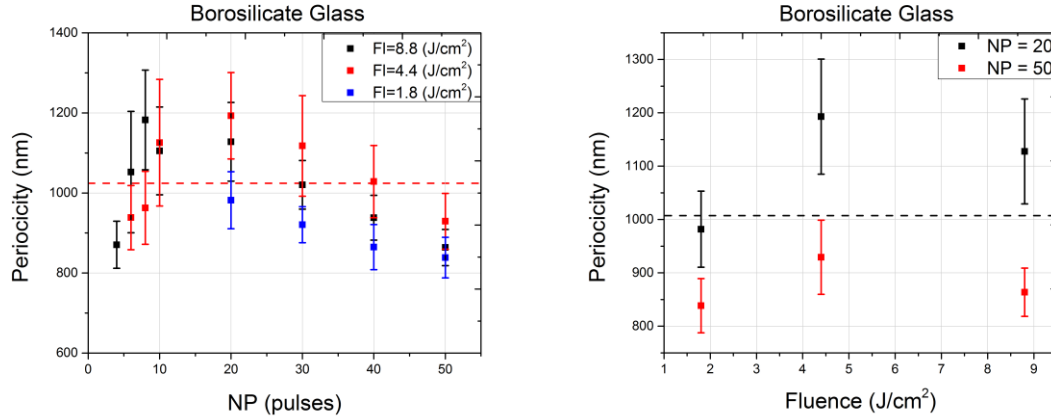


Figure 27: Borosilicate glass a) Periodic structure dependence on NP b) Fluence dependence of periodic structures for NP=20 (The red dash line indicates the wavelength of incident beam which is 1026nm).

3.3 LIPSS as a Function of Pulse Duration (PD)

The effect of pulse duration in LIPSS was explored. The results are presented in Fig. 28, 29 and 30 and we noticed that as the pulse duration decreases then the formation of LIPSS is in favor. In the case of PD = 10 ps only HSFL were observed and as the fluence and or number of pulses increases, a distraction of surface is observed without any formation of periodic structures. This is in agreement with the theoretical discussion in § 1.1.4 where as the pulse duration increases the thermalization process is becoming more intense. Also the peak power for PD = 10 ps decreases as the pulse stretches in time which leads to the formation of HSFL only. But as the fluence increases there is no formation of LSFL and grooves as in PD=170fs due to the distraction of the material.

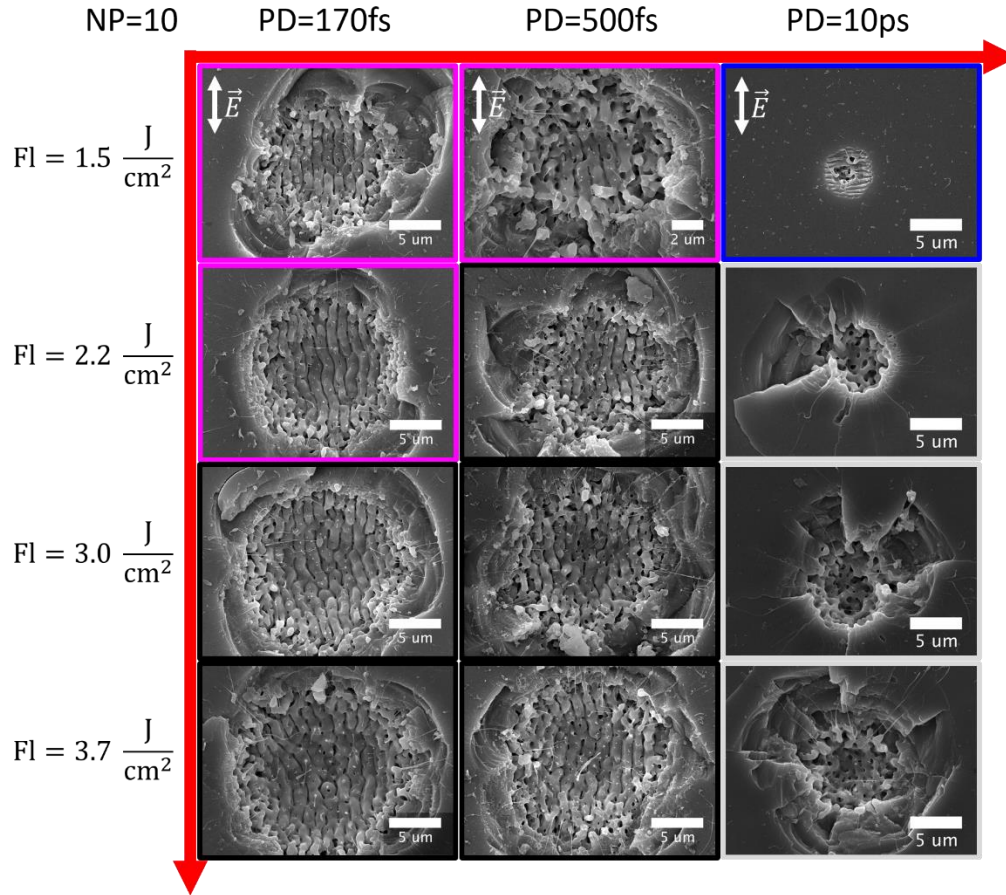


Figure 28: SEM images (Top view) of Fused silica after irradiation at 1026nm, NP=10 and RR=1kHz. Red arrows indicate the evolution of LIPPS as a function of Fluence and Pulse duration. Images are indicated by colors for HSFL (Blue), LSFL (Pink), Grooves (Black) and No structure formation (White)

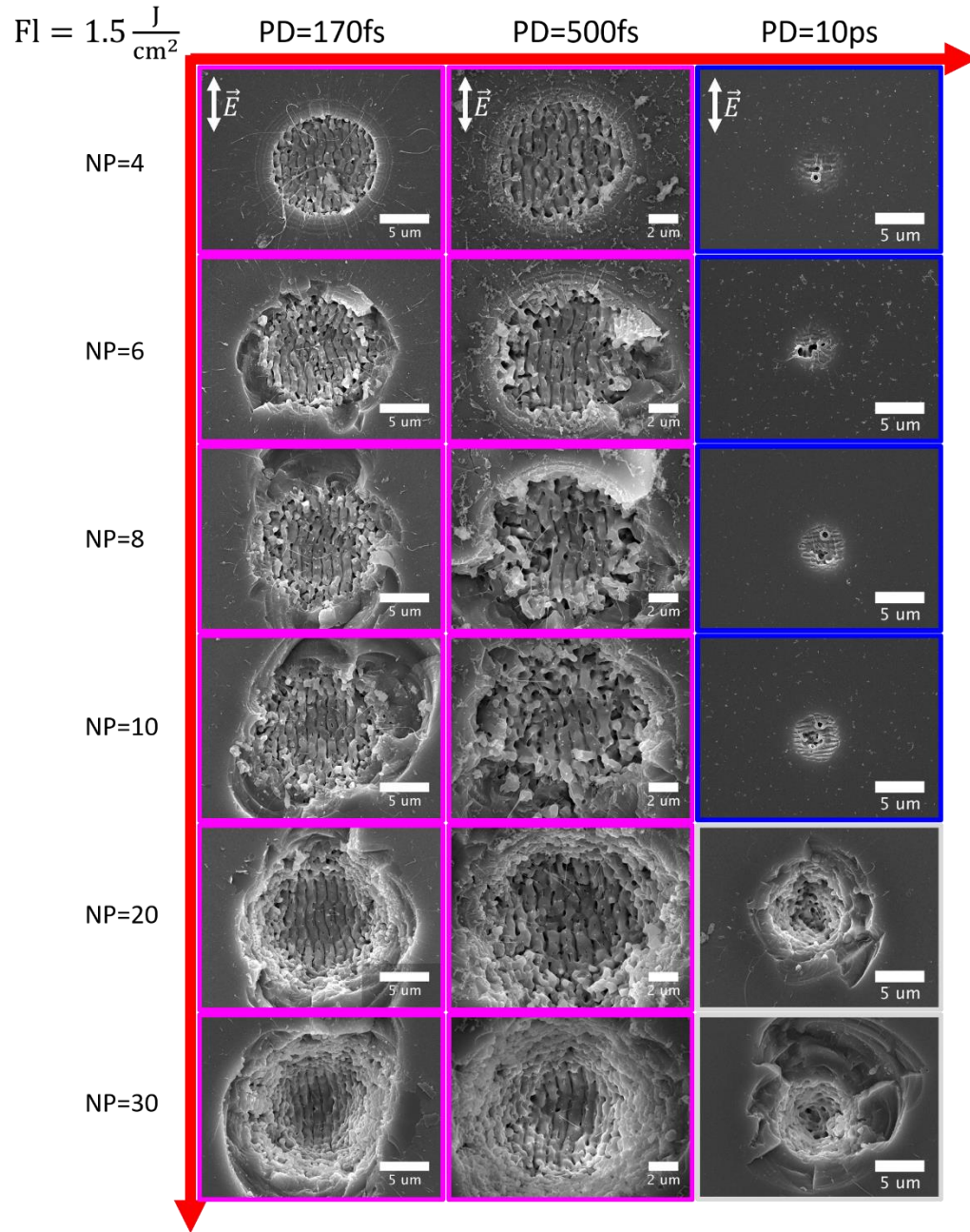


Figure 29: SEM images (Top view) of Fused silica after irradiation at 1026nm, $Fl=1.5 J/cm^2$ and $RR=1kHz$. Red arrows indicate the evolution of LIPPS as a function of Number of pulses and Pulse duration. Images are indicated by colors for HSFL (Blue), LSFL (Pink), Grooves (Black) and No structure formation (White)

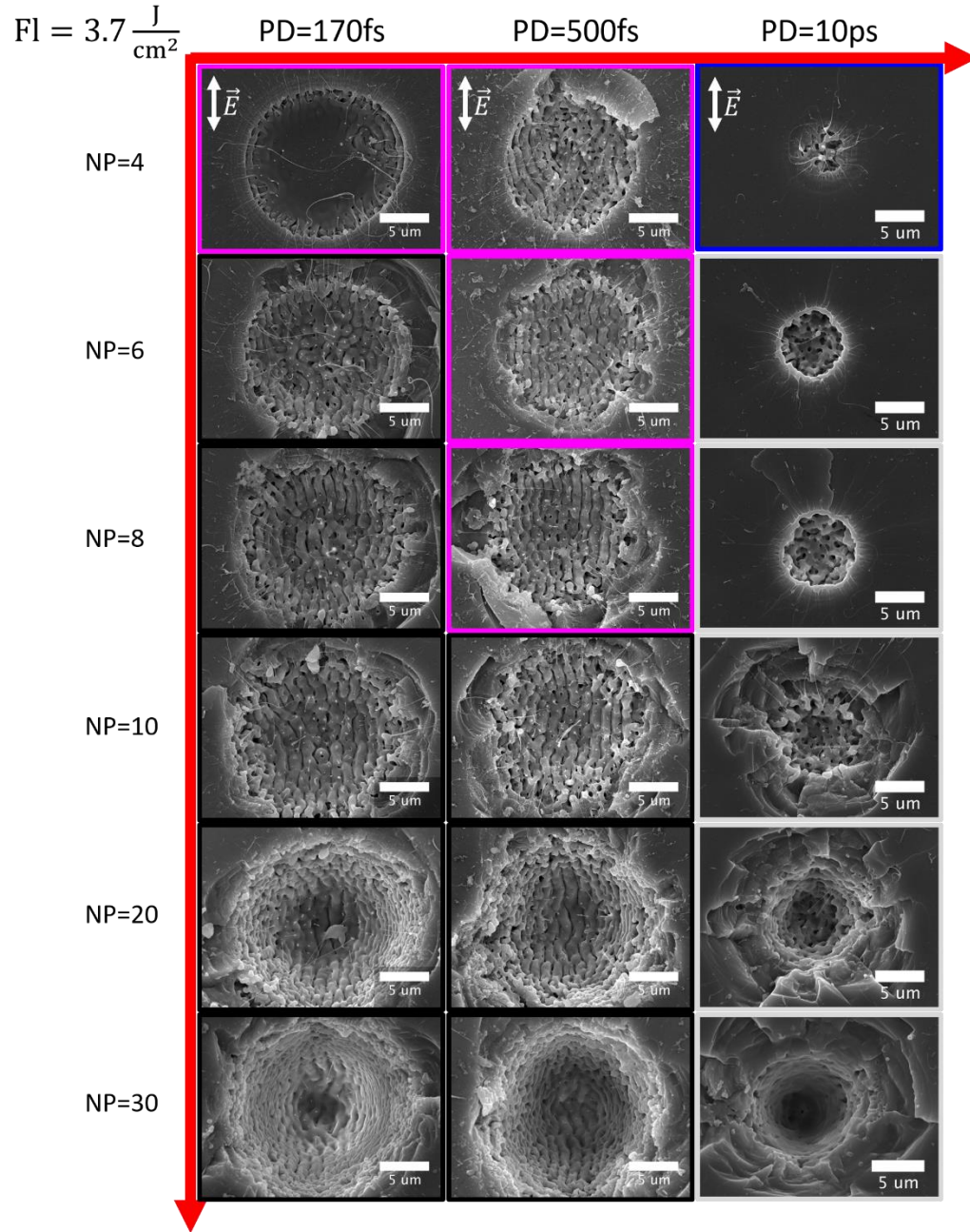


Figure 30: SEM images (Top view) of Fused silica after irradiation at 1026nm, $Fl=3.7 J/cm^2$ and $RR=1kHz$. Red arrows indicate the evolution of LIPPS as a function of Number of pulses and Pulse duration. Images are indicated by colors for HSFL (Blue), LSFL (Pink), Grooves (Black) and No structure formation (White)

3.4 Polarization Dependent LIPSS

The periodic structures formed after irradiation follow the polarization of the incident beam. Taking advantage of that we can use different polarization in order to create various types of

periodic structures. In this section we present the formation of ripples which are low spatial frequency LIPSS (LSFL) with periodicity near the wavelength $\lambda=1026$ nm. The structures are characterized with scanning electron microscopy (SEM) and as illustrated in Fig. 31 in all cases the ripples are oriented parallel to the polarization of the incident beam which is indicated with the red arrows. In the case of elliptical polarization the direction of periodic structures is parallel to the wide axis of the ellipse. Different kind of structures can be used in the field of biomimetics where the surface of a biological system can be reproduced in order to adopt a specific property of the surface.

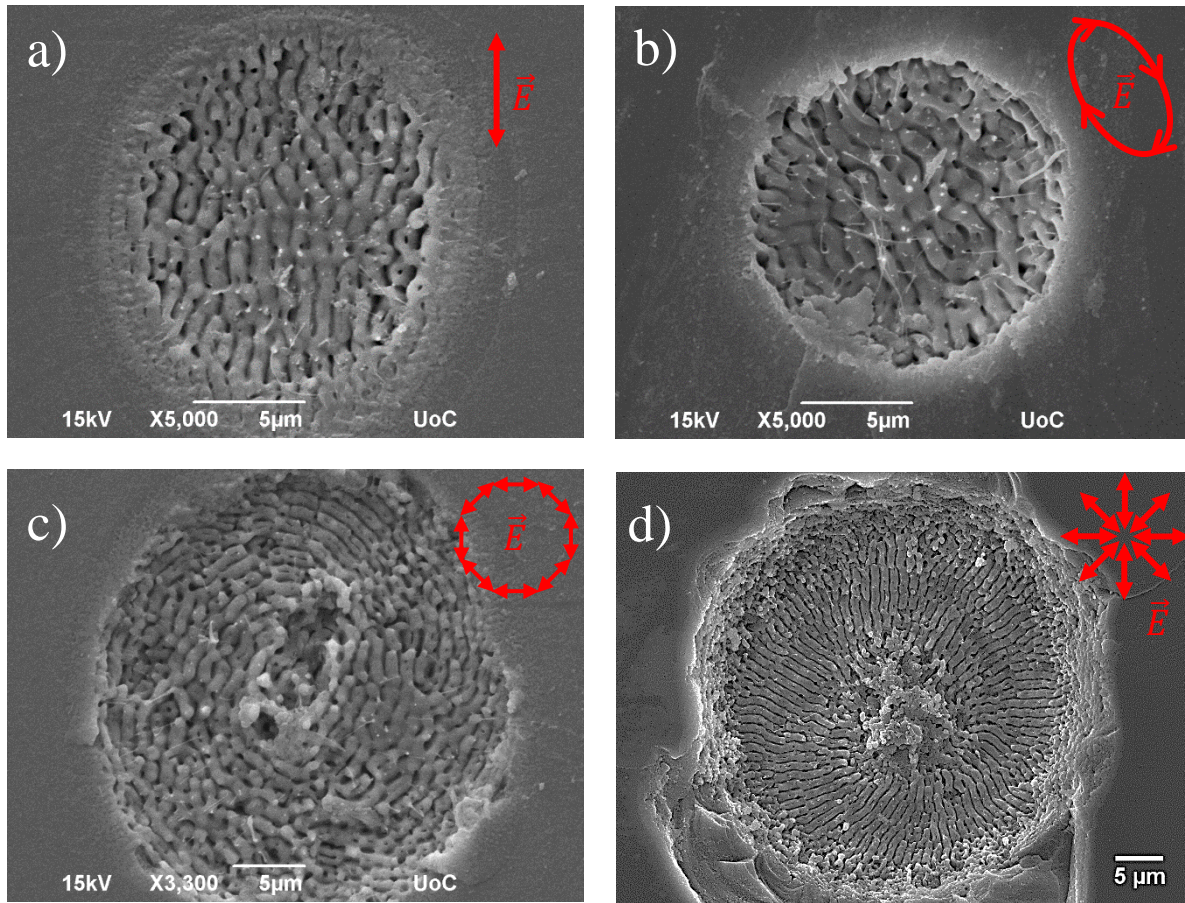


Figure 31: SEM images (Top view) on fused silica surface after irradiation at 1026nm, 170fs and 1kHz repetition rate with a) linear polarization, $Fl = 1.01 \frac{J}{cm^2}$, NP = 4 b) Elliptical polarization, $Fl = 0.76 \frac{J}{cm^2}$, NP = 4. c) Azimuthal polarization, $Fl = 3.97 \frac{J}{cm^2}$, NP = 4. d) Radial polarization, $Fl=4.7 \frac{J}{cm^2}$, NP = 6.

The periodicity of complex structures can also be manipulated by the NP and the fluence. In Fig. 32 the calculated periodicities are presented for elliptical, radial and azimuthal polarization.

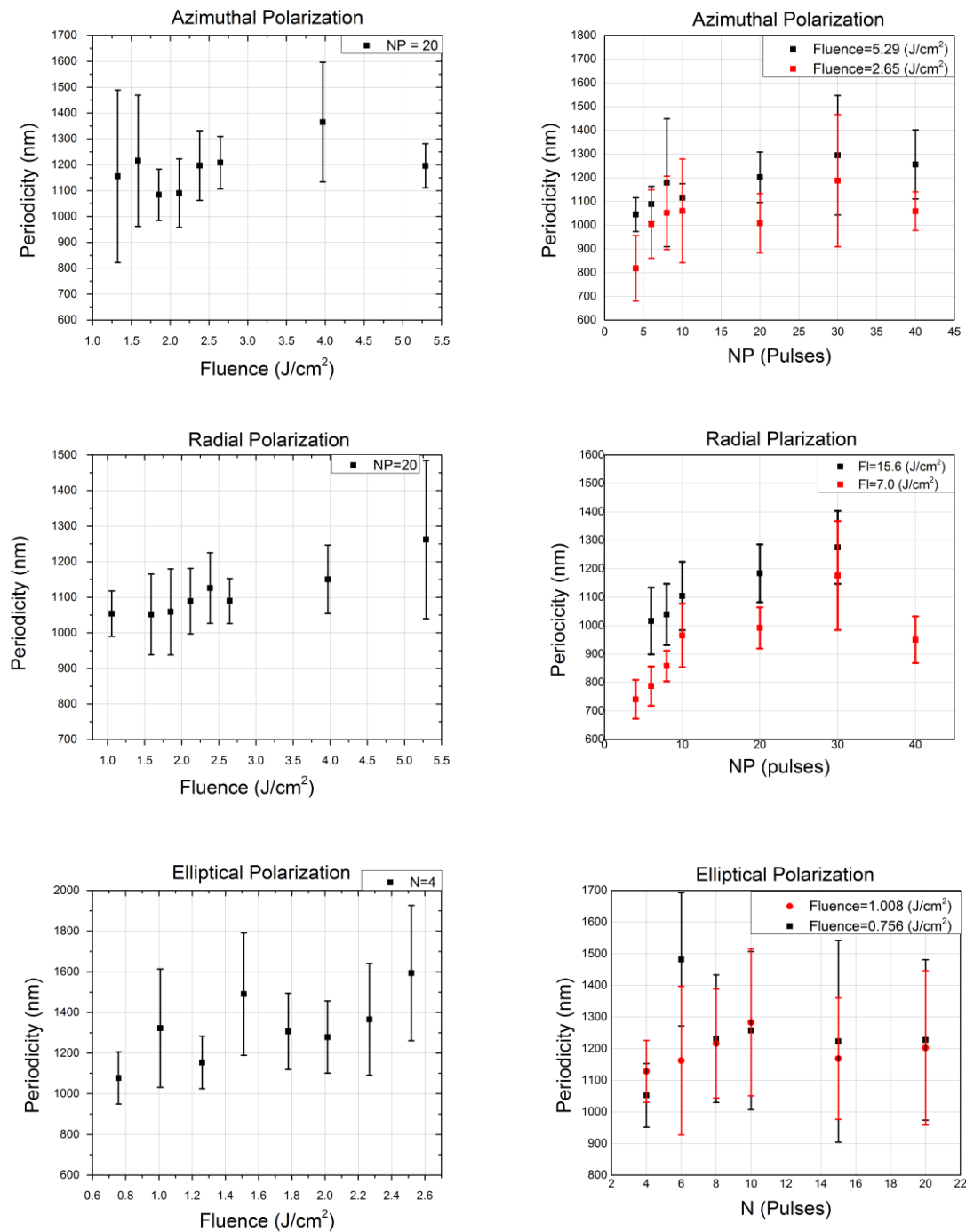


Figure 32: Periodicity dependence on NP and Fluence dependence of periodicity for azimuthal, radial and elliptical polarization.

3.5 Biomimetic surfaces

As discussed in § 1.1.5 the periodicity of Greta oto nanopillars is 100-140 nm, the radius is 40-60 nm and their height is 160-200 nm. In order to reproduce the pillars in the scale of nanometer it was necessary to work with periodic structures in the same scale as shown in Fig. 33 where the period is 359 ± 24 nm and belongs to the category of high spatial frequency LIPSS (HSFL).

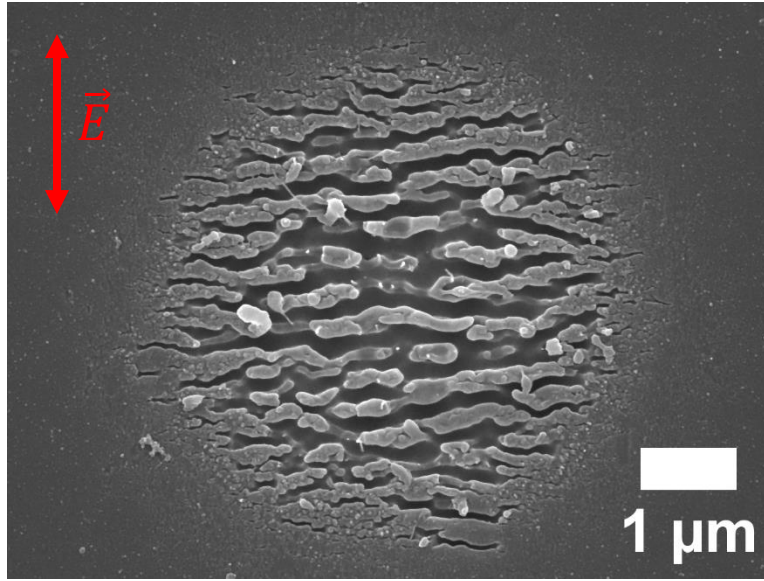


Figure 33: SEM images (Top view) on fused silica surface after irradiation at 1026nm and 60kHz repetition rate with linear polarization, $Fl=0.7 \frac{J}{cm^2}$, NP=15 and PD = 170 fs.

Relying on those structures, circular polarization was used instead for the formation of pillars in the same scale as butterfly nanopillars. For a circular polarization, a quarter-wave plate was used and the optical axis was set to 45 degrees as a function of the original polarization. In this section we present the formation of nanopillars as shown in Fig. 34, using circular polarization, which corresponds to HSFL in linear polarization Fig. 33.

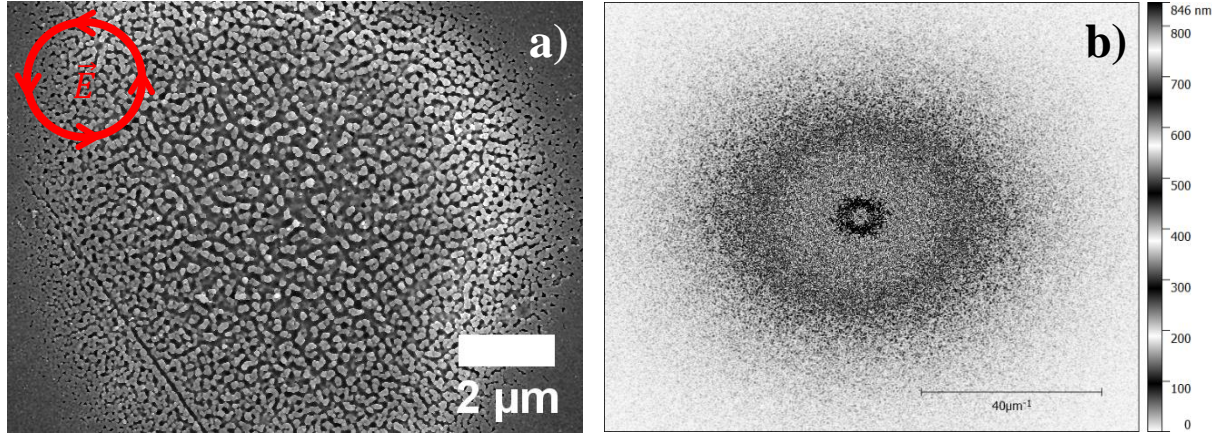


Figure 34: a) SEM images (Top view) on fused silica surface after irradiation at 1026nm and 1kHz repetition rate with circular polarization, PD = 170 fs, FI=12.57 $\frac{J}{cm^2}$, NP=6 and b) 2D-FFT of image (a)

The periodicity of nanopillars was calculated from the 2D-FFT and presented to Fig. 35a for the horizontal and vertical direction. The period is between the range of ~200-400 nm which is in the same order of butterfly's *Greta oto* nanopillars. The radius was also calculated and presented in Fig 35b which is in the range of ~80-120 nm.

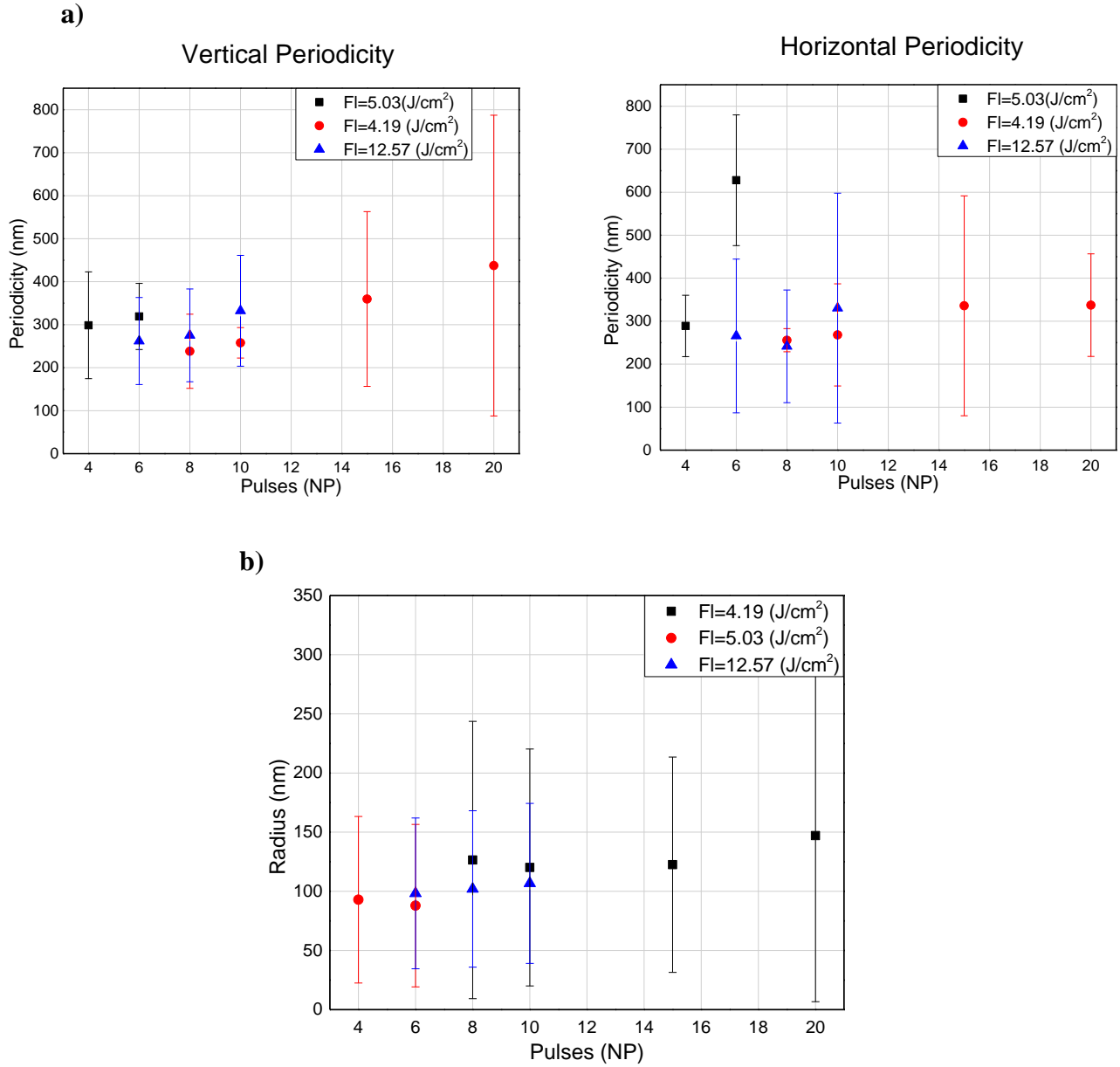


Figure 35: a) Nanopillars periodicity as a function of NP in vertical and horizontal direction. b) Nanopillar radius as a function of NP

The height of nanopillars was calculated to be 282 ± 42 nm from tilted SEM images presented in Fig. 36. That means that in all cases (periodicity, radius and height) the nanopillars LIPSS are twice the size compared to the butterfly's nanopillars but they are in the same order of magnitude.

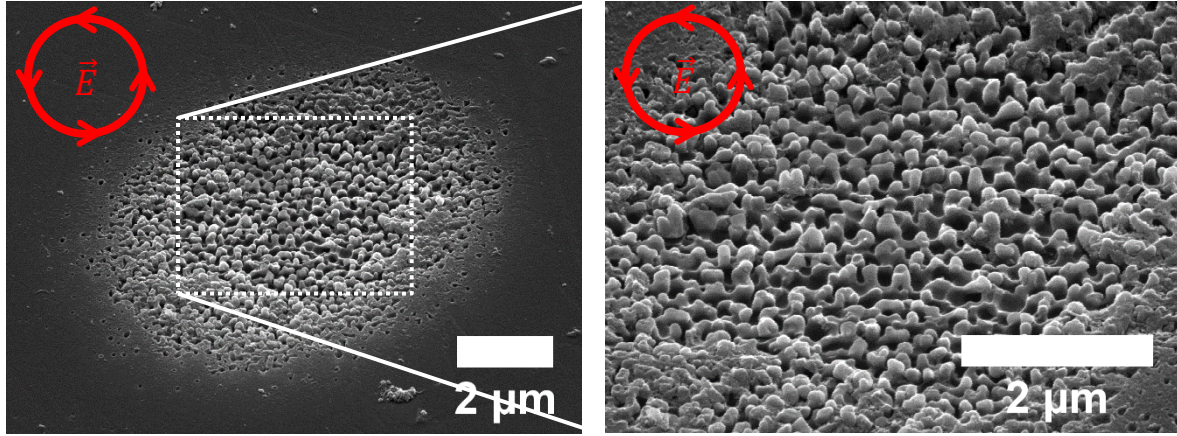


Figure 36: SEM images (45° tilted) on fused silica surface after irradiation at 1026nm and 1kHz repetition rate with circular polarization, 170 fs pulse duration $Fl=3.35 \frac{J}{cm^2}$, NP=10.

The next step is to reproduce those structures in a large scale area to review the optical properties and compare with the glasswing butterfly structures. To do that, a continuous pulsed beam with a circular polarization was used as well as a motorized stage for scanning the surface as show in Fig. 13. Due to the distraction of the surface when irradiating a defect of the surface, there were difficulties in producing large scale areas with nanopillars as shown in Fig. 37b and 37c.

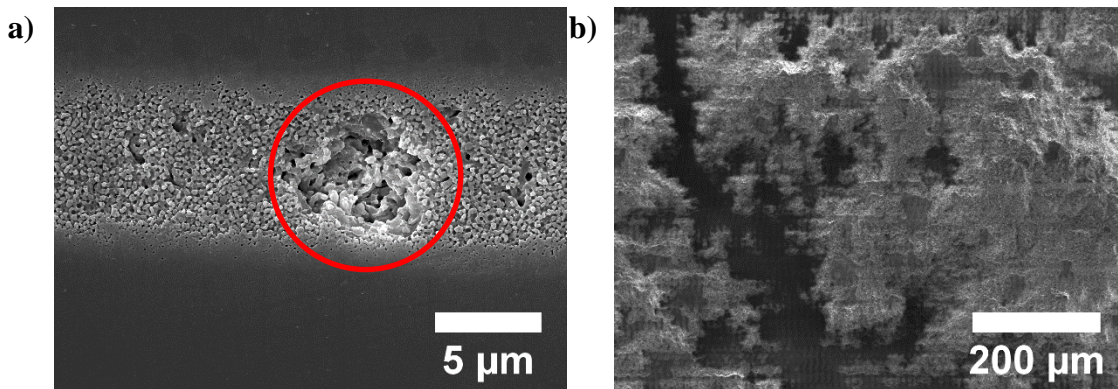


Figure 37: a) Damage spot during scanning b) Damage surface due to defects

A lot of effort has been made in order to reduce the damaged areas. In this section we present the results and the optical properties of the processed materials. Fig. 38a and 38b shows the transmittance and the reflectance of the processed surfaces in different y-step where y-step is the distance between the irradiating lines in micrometers. The speed of scanning is indicated in mm/s

and double side means that the material was processed in both surfaces. As the y-step decreases the reflectance decreases and the transparency increases for large wavelengths. For small wavelengths as the y-step decreases the reflectance tends to reach the flat surface and the transparency decreases dramatically. This means that the surface starts to absorb irradiation in the visible-UV spectrum which might be caused by the alternation of the chemical structure and the chemical composition.

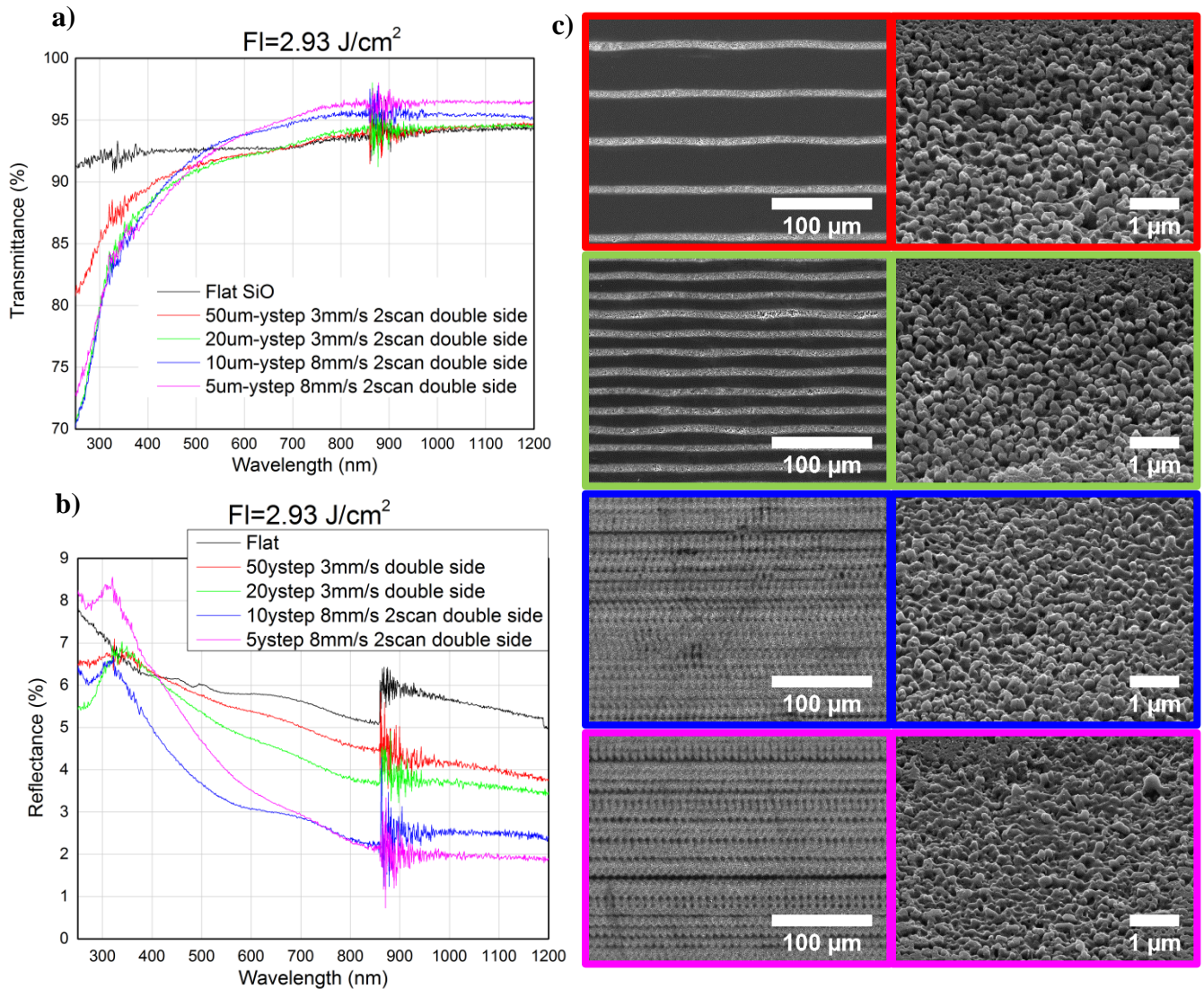


Figure 38: a) Transmittance spectrum b) Reflectance spectrum c) SEM images (top view and 40° tilted) of the surfaces indicated by the respectively colors of the spectrums.

Furthermore optical analysis has been conducted comparing processed single side materials with materials processed in both sides (indicated as double side). Materials processed in both sides present decreased reflectance and increased transmittance for large wavelengths. However, for small wavelength the transmittance is dramatically reduced.

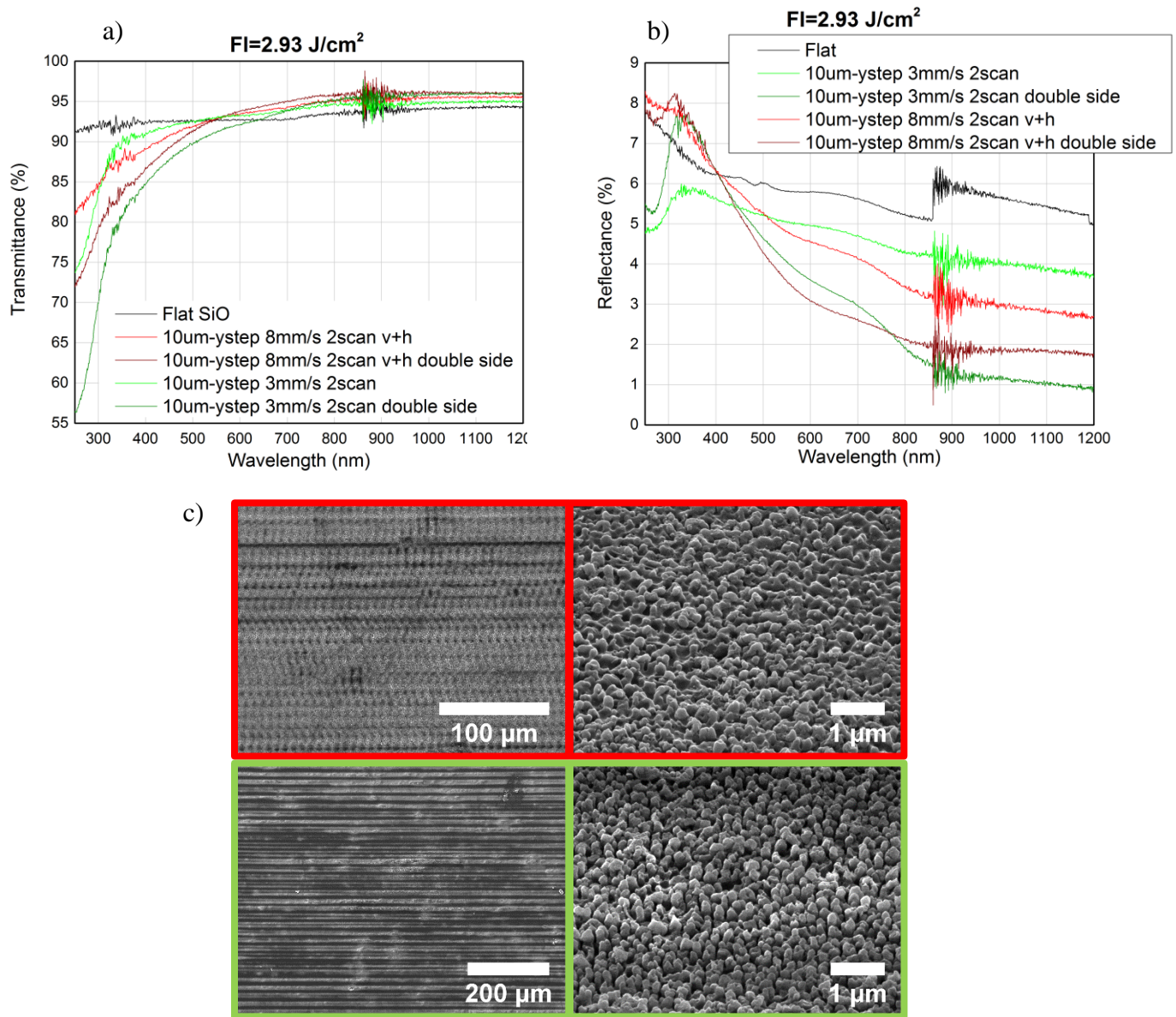


Figure 39: a) Transmittance spectrum for single and double side processing b) Reflectance spectrum for single and double side processing c) SEM images (top view and 40° tilted) of the surfaces indicated by the respectively colors of the spectrums.

Finally optical analysis has been made for different number of scans as shown in Fig. 40. The number of scans indicates how many times the overwriting irradiation was repeated. As the number of scans increases the reflectance decreases and the transparency increases for large wavelengths.

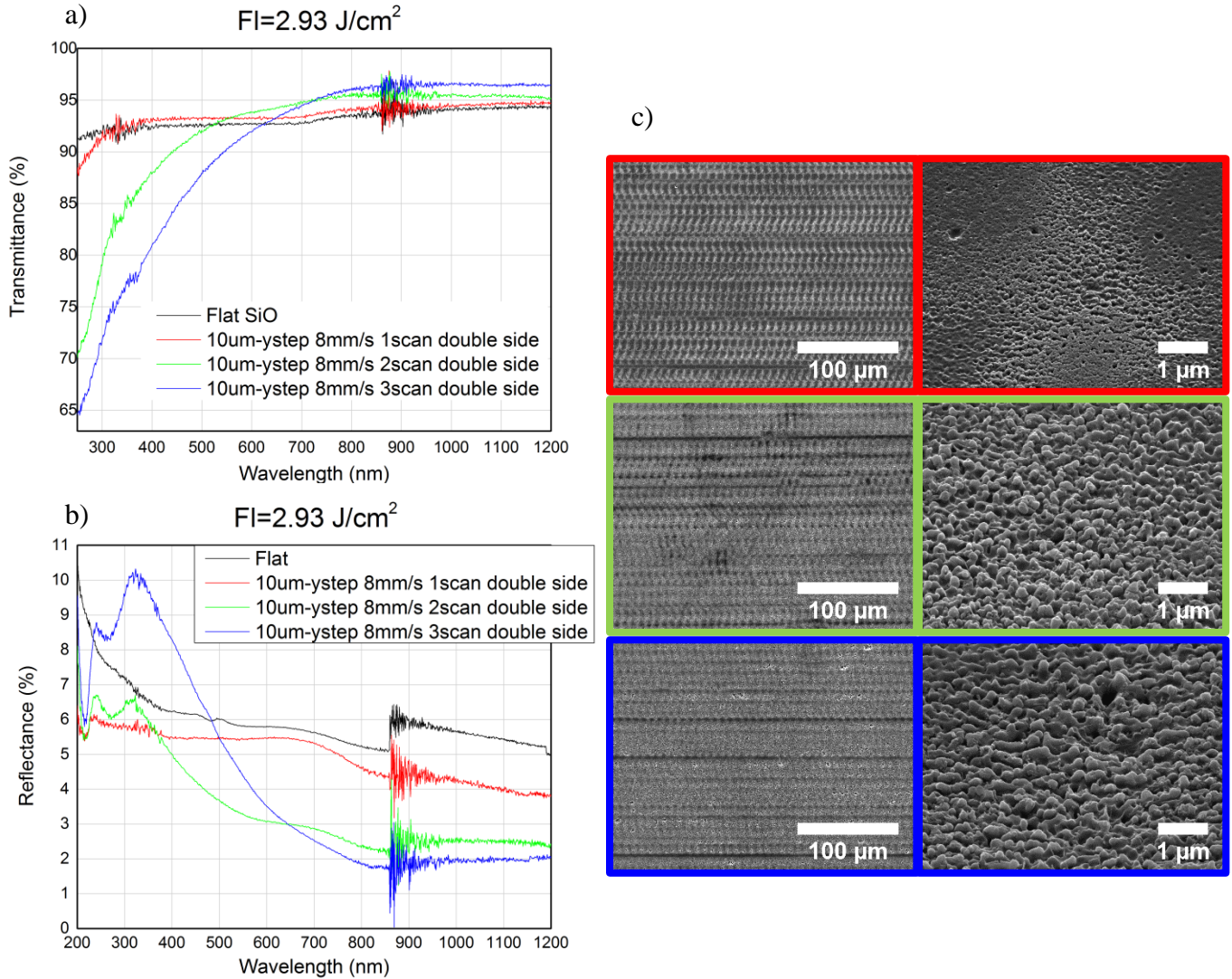


Figure 40: a) Transmittance spectrum for different number of scans b) Reflectance spectrum for different number of scans c) SEM images (top view and 40° tilted) of the surfaces indicated by the respectively colors of the spectrums.

Different sizes of nanopillar LIPSS can be produced by changing the wavelength of the incident irradiation. As shown in Fig. 41 the nanopillar LIPSS produced by 513nm wavelength irradiation are significantly smaller than the nanopillar LIPSS produced by 1026nm wavelength irradiation.

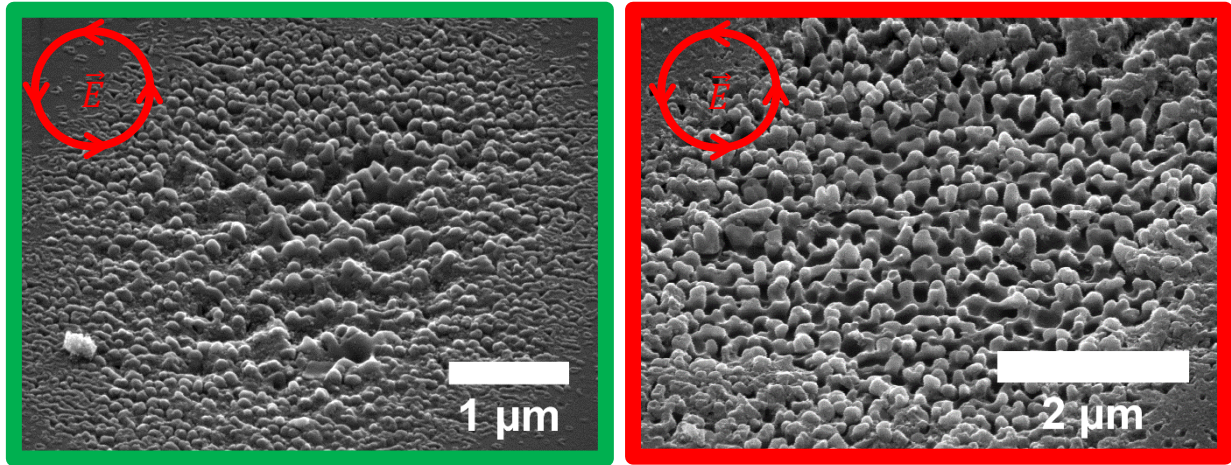


Figure 41: SEM images (45° tilted) on fused silica surface after irradiation a) at $\lambda=513\text{nm}$ where $\Lambda=376\pm35$ the periodicity, 52 ± 10 the radius and 156 ± 27 the height of nanopillars. b) at $\lambda=1026\text{nm}$ where $\Lambda=393\pm20$ the periodicity, 85 ± 17 the radius and 282 ± 42 the height of nanopillars.

CHAPTER 4: Conclusions

We have successfully fabricated periodic structures in a variety of orientations and periodicities by irradiating fused silica, soda-lime glass, borosilicate glass and quartz. We have concluded that the orientation of the structures depends on the polarization of the incident beam and more specifically LSFL and grooves are parallel to the polarization and HSFL are perpendicular to the polarization. Furthermore it's evident that the periodicity of those structures are affected by the fluence, wavelength and number of pulses. For future work we need to reproduce those structures in a large scale area for a variety of possible applications.

We have successfully fabricated nanopillars in fused silica using circular polarized electromagnetic beam. The morphological results showed that the periodicity, radius and height are usually two times larger than butterfly's Greta oto nanopillars however in the same magnitude of order. As shown in Fig 38, 39 and 40 can conclude that the fabricated nanopillars reduce the reflectance of the material in large wavelengths. On the contrary butterfly's nanopillars increase the reflectance in large wavelength as shown in Fig. 12. The divergence of the optical properties between the fabricated nanopillars and the glass wing butterfly nanopillars is assumed to depend on the following two reasons. First being the different type of the material and second being the difference in the size of the nanopillars. For future work it is imperative to reproduce those structures and analyze their optical properties in a variety of transparent materials. Finally an effort has to be made in order to reduce the size of nanopillars in large scale areas by using smaller wavelength of incident beam.

List of references

- [1] H.W. Mocker, R.J. Collins, MODE COMPETITION AND SELF-LOCKING EFFECTS IN A Q-SWITCHED RUBY LASER, *Applied Physics Letters*, 7 (1965) 270-273.
- [2] E. Goulielmakis, M. Schultze, M. Hofstetter, V.S. Yakovlev, J. Gagnon, M. Uiberacker, A.L. Aquila, E.M. Gullikson, D.T. Attwood, R. Kienberger, F. Krausz, U. Kleineberg, Single-Cycle Nonlinear Optics, *Science*, 320 (2008) 1614-1617.
- [3] M.E. Fermann, A. Galvanauskas, G. Sucha, *Ultrafast Lasers: Technology and Applications*, Taylor & Francis, 2003.
- [4] M. Birnbaum, Semiconductor Surface Damage Produced by Ruby Lasers, *Journal of Applied Physics*, 36 (1965) 3688-3689.
- [5] J.P. Colombier, F. Garrelie, N. Faure, S. Reynaud, M. Bounhalli, E. Audouard, R. Stoian, F. Pigeon, Effects of electron-phonon coupling and electron diffusion on ripples growth on ultrafast-laser-irradiated metals, *Journal of Applied Physics*, 111 (2012) 024902.
- [6] A.Y. Vorobyev, C. Guo, Femtosecond laser-induced periodic surface structure formation on tungsten, *Journal of Applied Physics*, 104 (2008) 063523.
- [7] J. Wang, C. Guo, Numerical study of ultrafast dynamics of femtosecond laser-induced periodic surface structure formation on noble metals, *Journal of Applied Physics*, 102 (2007) 053522.
- [8] J. Wang, C. Guo, Ultrafast dynamics of femtosecond laser-induced periodic surface pattern formation on metals, *Applied Physics Letters*, 87 (2005) 251914.
- [9] K. Lou, S.-X. Qian, X.-L. Wang, Y. Li, B. Gu, C. Tu, H.-T. Wang, Two-dimensional microstructures induced by femtosecond vector light fields on silicon, *Opt. Express*, 20 (2012) 120-127.
- [10] A. Borowiec, H.K. Haugen, Subwavelength ripple formation on the surfaces of compound semiconductors irradiated with femtosecond laser pulses, *Applied Physics Letters*, 82 (2003) 4462-4464.
- [11] M. Barberoglou, V. Zorba, E. Stratakis, E. Spanakis, P. Tzanetakis, S.H. Anastasiadis, C. Fotakis, Bio-inspired water repellent surfaces produced by ultrafast laser structuring of silicon, *Applied Surface Science*, 255 (2009) 5425-5429.
- [12] S.K. Das, H. Messaoudi, A. Debroy, E. McGlynn, R. Grunwald, Multiphoton excitation of surface plasmon-polaritons and scaling of nanoripple formation in large bandgap materials, *Opt. Mater. Express*, 3 (2013) 1705-1715.
- [13] K. Kawamura, T. Ogawa, N. Sarukura, M. Hirano, H. Hosono, Fabrication of surface relief gratings on transparent dielectric materials by two-beam holographic method using infrared femtosecond laser pulses, *Appl Phys B*, 71 (2000) 119-121.
- [14] S.S. Mao, F. Quéré, S. Guizard, X. Mao, R.E. Russo, G. Petite, P. Martin, Dynamics of femtosecond laser interactions with dielectrics, *Appl Phys A*, 79 (2004) 1695-1709.
- [15] S. Matsuo, S. Hashimoto, Spontaneous formation of 10- μ m-scale periodic patterns in transverse-scanning femtosecond laser processing, *Opt. Express*, 23 (2015) 165-171.
- [16] W.E. Lamb, Theory of an Optical Maser, *Physical Review*, 134 (1964) A1429-A1450.
- [17] B.K. Garside, T.K. Lim, Laser mode locking using saturable absorbers, *Journal of Applied Physics*, 44 (1973) 2335-2342.
- [18] A. Yariv, Internal Modulation in Multimode Laser Oscillators, *Journal of Applied Physics*, 36 (1965) 388-391.
- [19] D. Strickland, G. Mourou, Compression of amplified chirped optical pulses, *Optics Communications*, 55 (1985) 447-449.
- [20] G.L. Tan, M.F. Lemon, D.J. Jones, R.H. French, Optical properties and London dispersion interaction of amorphous and crystalline SiO₂ determined by vacuum ultraviolet spectroscopy and spectroscopic ellipsometry, *Physical Review B*, 72 (2005) 205117.

- [21] B.H.W.S. De Jong, R.G.C. Beerkens, P.A. van Nijnatten, Glass, in: Ullmann's Encyclopedia of Industrial Chemistry, Wiley-VCH Verlag GmbH & Co. KGaA, 2000.
- [22] I.H. Malitson, Interspecimen Comparison of the Refractive Index of Fused Silica*,†, J. Opt. Soc. Am., 55 (1965) 1205-1209.
- [23] W.A. Gambling, The rise and rise of optical fibers, IEEE Journal of Selected Topics in Quantum Electronics, 6 (2000) 1084-1093.
- [24] N. Doğan Baydoğan, A.B. Tuğrul, Evaluation of the optical changes for a soda-lime-silicate glass exposed to radiation, Glass Physics and Chemistry, 32 (2006) 309-314.
- [25] M. Rubin, Optical properties of soda lime silica glasses, Solar Energy Materials, 12 (1985) 275-288.
- [26] H.L.S.a.A.J. Cohen, Absorption spectra of cations in alkali-silicate glasses of high ultra-violet transmission, Physics and Chemistry of Glasses, 4 (1963) 173-187.
- [27] D.J. Little, M. Ams, M.J. Withford, Influence of bandgap and polarization on photo-ionization: guidelines for ultrafast laser inscription [Invited], Opt. Mater. Express, 1 (2011) 670-677.
- [28] G. Ghosh, Dispersion-equation coefficients for the refractive index and birefringence of calcite and quartz crystals, Optics Communications, 163 (1999) 95-102.
- [29] G.W. Pierce, Piezoelectric Crystal Resonators and Crystal Oscillators Applied to the Precision Calibration of Wavemeters, Proceedings of the American Academy of Arts and Sciences, 59 (1923) 81-106.
- [30] L. V.KELDysh, IONIZATION IN THE FIELD OF A STRONG ELECTROMAGNETIC WAVE, SOVIET PHYSICS JETP, 20 (1965) 1307
- [31] B.S. Chris, B. André, M. Eric, Laser-induced breakdown and damage in bulk transparent materials induced by tightly focused femtosecond laser pulses, Measurement Science and Technology, 12 (2001) 1784.
- [32] Y.C. Koji Sugioka, Ultrafast Laser Processing: From Micro- to Nanoscale, 2013.
- [33] R.R. Gattass, E. Mazur, Femtosecond laser micromachining in transparent materials, Nat Photon, 2 (2008) 219-225.
- [34] K.C. Phillips, H.H. Gandhi, E. Mazur, S.K. Sundaram, Ultrafast laser processing of materials: a review, Adv. Opt. Photon., 7 (2015) 684-712.
- [35] L. Jiang, X. Shi, X. Li, Y. Yuan, C. Wang, Y. Lu, Subwavelength ripples adjustment based on electron dynamics control by using shaped ultrafast laser pulse trains, Opt. Express, 20 (2012) 21505-21511.
- [36] D. Dufft, A. Rosenfeld, S.K. Das, R. Grunwald, J. Bonse, Femtosecond laser-induced periodic surface structures revisited: A comparative study on ZnO, Journal of Applied Physics, 105 (2009) 034908.
- [37] S. Höhm, A. Rosenfeld, J. Krüger, J. Bonse, Femtosecond diffraction dynamics of laser-induced periodic surface structures on fused silica, Applied Physics Letters, 102 (2013) 054102.
- [38] G. Seifert, M. Kaempfe, F. Syrowatka, C. Harnagea, D. Hesse, H. Graener, Self-organized structure formation on the bottom of femtosecond laser ablation craters in glass, Appl Phys A, 81 (2005) 799-803.
- [39] G.D. Tsibidis, E. Skoulas, A. Papadopoulos, E. Stratakis, Convection roll-driven generation of supra-wavelength periodic surface structures on dielectrics upon irradiation with femtosecond pulsed lasers, Physical Review B, 94 (2016) 081305.
- [40] Y. Han, X. Zhao, S. Qu, Polarization dependent ripples induced by femtosecond laser on dense flint (ZF6) glass, Opt. Express, 19 (2011) 19150-19155.
- [41] X. Shi, L. Jiang, X. Li, S. Wang, Y. Yuan, Y. Lu, Femtosecond laser-induced periodic structure adjustments based on electron dynamics control: from subwavelength ripples to double-grating structures, Opt. Lett., 38 (2013) 3743-3746.
- [42] G.D. Tsibidis, M. Barberoglou, P.A. Loukakos, E. Stratakis, C. Fotakis, Dynamics of ripple formation on silicon surfaces by ultrashort laser pulses in subablation conditions, Physical Review B, 86 (2012) 115316.
- [43] B. Rethfeld, Free-electron generation in laser-irradiated dielectrics, Physical Review B, 73 (2006) 035101.

- [44] M.K. Smith, S.H. Davis, Instabilities of Dynamic Thermocapillary Liquid Layers .1. Convective Instabilities, *Journal of Fluid Mechanics*, 132 (1983) 119-144.
- [45] A.E. Hosoi, J.W.M. Bush, Evaporative instabilities in climbing films, *Journal of Fluid Mechanics*, 442 (2001) 217-239.
- [46] F.H. Busse, Non-linear properties of thermal convection, *Reports on Progress in Physics*, 41 (1978) 1929.
- [47] V. Zorba, E. Stratakis, M. Barberoglou, E. Spanakis, P. Tzanetakis, S.H. Anastasiadis, C. Fotakis, Biomimetic Artificial Surfaces Quantitatively Reproduce the Water Repellency of a Lotus Leaf, *Advanced Materials*, 20 (2008) 4049-4054.
- [48] E. Stratakis, A. Ranella, C. Fotakis, Biomimetic micro/nanostructured functional surfaces for microfluidic and tissue engineering applications, *Biomicrofluidics*, 5 (2011) 013411.
- [49] K. Haupt, K. Mosbach, Molecularly Imprinted Polymers and Their Use in Biomimetic Sensors, *Chemical Reviews*, 100 (2000) 2495-2504.
- [50] R.H. Siddique, G. Gomard, H. Holscher, The role of random nanostructures for the omnidirectional anti-reflection properties of the glasswing butterfly, *Nat Commun*, 6 (2015).
- [51] S. Chattopadhyay, Y.F. Huang, Y.J. Jen, A. Ganguly, K.H. Chen, L.C. Chen, Anti-reflecting and photonic nanostructures, *Materials Science and Engineering: R: Reports*, 69 (2010) 1-35.
- [52] H.K. Raut, V.A. Ganesh, A.S. Nair, S. Ramakrishna, Anti-reflective coatings: A critical, in-depth review, *Energy & Environmental Science*, 4 (2011) 3779-3804.
- [53] J. Cai, L. Qi, Recent advances in antireflective surfaces based on nanostructure arrays, *Materials Horizons*, 2 (2015) 37-53.